Injection of Fluids into Supercritical Environments

M. Oschwald, J.J. Smith, R. Branam, J. Hussong, A. Schik
German Aerospace Center (DLR), Institute of Space Propulsion Lampoldshausen

*B. Chehroudi, D. Talley
U.S. Air Force Research Laboratory (AFRL), Propulsion Directorate
*Engineering Research Consultant

2 September 2004

<table>
<tr><td colspan="3" align="center">Report Documentation Page</td><td>Form Approved
OMB No. 0704-0188</td></tr>
</table>

Report Documentation Page			*Form Approved* *OMB No. 0704-0188*

Public reporting burden for the collection of information is estimated to average 1 hour per response, including the time for reviewing instructions, searching existing data sources, gathering and maintaining the data needed, and completing and reviewing the collection of information. Send comments regarding this burden estimate or any other aspect of this collection of information, including suggestions for reducing this burden, to Washington Headquarters Services, Directorate for Information Operations and Reports, 1215 Jefferson Davis Highway, Suite 1204, Arlington VA 22202-4302. Respondents should be aware that notwithstanding any other provision of law, no person shall be subject to a penalty for failing to comply with a collection of information if it does not display a currently valid OMB control number.

1. REPORT DATE **14 JUN 2004**	2. REPORT TYPE	3. DATES COVERED **-**

4. TITLE AND SUBTITLE **Injection of Fluids into Supercritical Environments**	5a. CONTRACT NUMBER
	5b. GRANT NUMBER
	5c. PROGRAM ELEMENT NUMBER
6. AUTHOR(S) **M Oschwald; J Smith; R Branam; J Hussong; A Schik**	5d. PROJECT NUMBER **2308**
	5e. TASK NUMBER **M13C**
	5f. WORK UNIT NUMBER

7. PERFORMING ORGANIZATION NAME(S) AND ADDRESS(ES) **Air Force Research Laboratory (AFMC),AFRL/PRSA,10 E. Saturn Blvd.,Edwards AFB,CA,93524-7680**	8. PERFORMING ORGANIZATION REPORT NUMBER

9. SPONSORING/MONITORING AGENCY NAME(S) AND ADDRESS(ES)	10. SPONSOR/MONITOR'S ACRONYM(S)
	11. SPONSOR/MONITOR'S REPORT NUMBER(S)

12. DISTRIBUTION/AVAILABILITY STATEMENT
Approved for public release; distribution unlimited

13. SUPPLEMENTARY NOTES

14. ABSTRACT

This paper summarizes and compares the results of systematic research programs at two independent labo-ratories regarding the injection of cryogenic liquids at subcritical and supercritical pressures, with applica-tion to liquid rocket engines. Both single jets and coaxial jets have been studied. Cold flow studies pro-vided valuable information without introducing the complexities of combustion. Initial studies utilized a single jet of cryogenic nitrogen injected into a quiescent room temperature nitrogen environment with pressures below and above the thermodynamic critical pressure of the nitrogen. Later, the work was ex-tended to investigate the effects of a co-flowing gas. Parallel to this work, combustion studies with cryo-genic propellants were introduced to understand high pressure coaxial injection phenomena with the influ-ence of chemical reaction. Shadowgraphy and spontaneous Raman scattering were used to measure quanti-ties such as growth rates, core lengths, turbulent length scales, fractal dimensions, and jet breakup regimes. It is found that jets injected at supercritical pressures do not atomize as they do at subcritical pressures. Rather, they behave in many respects like variable density turbulent gas jets.

15. SUBJECT TERMS

16. SECURITY CLASSIFICATION OF:			17. LIMITATION OF ABSTRACT	18. NUMBER OF PAGES **44**	19a. NAME OF RESPONSIBLE PERSON
a. REPORT **unclassified**	b. ABSTRACT **unclassified**	c. THIS PAGE **unclassified**			

Standard Form 298 (Rev. 8-98)
Prescribed by ANSI Std Z39-18

Abstract

This paper summarizes and compares the results of systematic research programs at two independent laboratories regarding the injection of cryogenic liquids at subcritical and supercritical pressures, with application to liquid rocket engines. Both single jets and coaxial jets have been studied. Cold flow studies provided valuable information without introducing the complexities of combustion. Initial studies utilized a single jet of cryogenic nitrogen injected into a quiescent room temperature nitrogen environment with pressures below and above the thermodynamic critical pressure of the nitrogen. Later, the work was extended to investigate the effects of a co-flowing gas. Parallel to this work, combustion studies with cryogenic propellants were introduced to understand high pressure coaxial injection phenomena with the influence of chemical reaction. Shadowgraphy and spontaneous Raman scattering were used to measure quantities such as growth rates, core lengths, turbulent length scales, fractal dimensions, and jet breakup regimes. It is found that jets injected at supercritical pressures do not atomize as they do at subcritical pressures. Rather, they behave in many respects like variable density turbulent gas jets.

1   Introduction

In recent years, laboratories at the German Aerospace Center (DLR) and the Air Force Research Laboratory (AFRL) have both conducted independent studies of the injection of cryogenic liquids at subcritical and supercritical pressures, with application to liquid rocket engines. In some instances, the studies involved were similar, allowing conclusions to be drawn regarding the degree to which the results at each laboratory corroborate each other. In other instances, studies at one laboratory extended beyond what was done at the other, allowing a breadth of scope which would not have been possible at either laboratory by itself. The purpose of this joint paper is to consolidate and compare the findings of both laboratories to date in a single place.

In what follows, background material regarding high pressure combustion in liquid rocket engines and thermophysical properties is provided in order to be better able to interpret the results to be presented subsequently. Following that, descriptions of the test benches and optical diagnostics are given, again in sufficient detail to be able to interpret the results to be presented subsequently. Next, results pertaining simple round jets are systematically presented, followed by a systematic extension to more complex coaxial jets more representative of liquid rocket engine injectors. Emphasis is placed throughout on the change in phenomenology of the jets as pressure is increased from subcritical to supercritical values. A summary and conclusions section completes the paper.

1.1   High pressure combustion in liquid rocket engines

By a simple thermodynamic analysis of a liquid rocket engine thrust chamber, it can be shown that higher chamber pressures allow a higher specific impulse for the engine to be produced. Higher chamber pressures similarly increase the power output and efficiency of gas turbines and diesel engines. This has motivated a general trend towards increasingly higher chamber pressures in propulsion applications. However, at higher pressures, the injected propellant can and often does find itself near or above the thermodynamic critical pressure. Table 1 shows the chamber pressures of several current liquid rocket engines which use liquid oxygen (LOX) and hydrogen as propellants, including the Space Shuttle Main Engine (SSME) and the Vulcain engine which powers the Ariane 5 launch vehicle. The chamber pressures are shown relative to the critical pressure of oxygen. It can be seen that all of the chamber pressures are supercritical relative to oxygen. Table 2 gives the critical properties of several relevant fluids.

In rocket applications, fluids injected into a supercritical ambient pressure often possess a subcritical initial temperature. The jet is then heated up beyond its critical temperature as it mixes and burns in the combustion chamber, a process which has sometimes been called "transcritical" injection. Prior to the systematic investigations started by the DLR and AFRL laboratories, little reliable information existed on how jet behavior may change as the pressure is increased from a subcritical to a supercritical value. The main objective of these investigations was to provide a better understanding of atomization, mixing, flow dynam-

ics, and flame stabilization for high pressure subcritical and supercritical jets. It is expected that these will lead to enhanced physical models for an improved design methodology.

1.2   Thermophysical properties and issues specific to transcritical inje ction

In this section, the behavior of relevant thermophysical properties is discussed. For coaxial injection of O_2 and H_2 in a liquid rocket engine, the oxygen is typically injected at a cold, subcritical temperature, with a liquid-like density through the center post, while the hydrogen, which is typically used to first cool the engine nozzle, is injected at a warm, supercritical temperature with a gas-like density in the annular pas-sage. The propellants then mix and burn in the resulting shear layer. Under these conditions, caution must be used when referring to the thermodynamic state of the fluids. At elevated pressures, the solubility of the gas in the liquid can be substantially increased, and it becomes necessary to consider the critical properties of a mixture. A single critical "point" then no longer exists; instead, critical mixing lines define the the r-modynamic state. In general, the critical properties of a mixture shift relative to the critical properties of any of its constit uents.

The phase diagram for the binary H_2/O_2-system is shown in Fig. 1. For a given reduced pressure $P_r = P_{ch}/P_{critO2}$, there is a critical mixing temperature above which the mixture is in a supercritical state. Be-low the critical mixing temperature, a binary system separates into liquid and gaseous phases. At a given temperature, the two phases are identified by the dashed and solid lines for the gaseous and liquid comp o-nents, respectively. As seen in Fig. 1, the solubility of H_2 in the liquid O_2 increases with an increase in temperature, whereas the amount of the hydrogen in the gaseous phase mixture decreases (see the dashed curve). At the critical mixing temperature, the mole fractions of each species in the gaseous and liquid phases are identical, the phase boundary disappears, and a supercritical condition exists.

Figure 2 shows the critical mixing temperature as a function of pressure for the various binary systems of interest. Below the critical mixing temperature, phase equilibrium between the liquid and gas exists. Above this temperature, the mixture exhibits supercritical behavior. The general trend is that the critical mixing temperature decreases with increasing pressure.

The surface tension of a binary H_2/O_2 mixture has been computed using the Macleod-Sugdon correlation (see Tully et al. (1970) and Macleod (1923)), and is shown in Fig. 3. The results indicate that at pressures above the critical pressure of pure O_2, surface tension may still be present in the binary H_2/O_2 system, as long as the temperature remains below the critical mixing temperature. This is of course consistent with the fact that the phase diagram in Fig. 1 predicts two phases for these conditions.

At pressures near the critical pressure, fluid properties become very sensitive to changes in temperature. The variation of density as a function of temperature is shown in Fig. 4 for pure nitrogen at a pressure of 4 MPa, which is a little greater than the critical pressure (3.4 MPa) of nitrogen. At a temperature of 129 K, the density of the nitrogen varies by up to 21% per degree Kelvin. The specific heat is also shown in Fig. 4 to increase precipitously by nearly an order of magnitude as temperature increases, reaching a distinct maximum at a temperature of 129.5 K in this example, and then it decreases again equally as precip i-tously. The temperature at which the specific heat reaches a maximum will be designated her as T*. When the pressure is equal to the critical pressure, the temperature T* is equal to the critical temperature, and the specific heat becomes infinite. At pressures greater than the critical pressure, the specific heat can no longer become infinite, but a maximum is still reached. Near the critical pressure, the maximum can be quite pronounced, as it is in Fig. 4, but reduces in significance as pressure increases. A plot of T* as a function of pressure is shown as the dashed line in Fig. 5. Also plotted as a solid line in Fig. 5 is the two phase coexistence line at lower pressures. The dashed (T*, P) curve is seen to form a continuation of the solid two phase coexistence line; for this and other reasons to be discussed later it is called here the "pseudo-boiling" line. Also shown in Fig. 5 is a contour plot of the thermal diffusivity. It can be seen that when the temperature is equal to T*, where the specific heat is at its maximum, the thermal diffusivity

reaches a distinct minimum. Variations such as these have distinct consequences for the transport of sp e-cies and energy, as results will illustrate further later.

2 Test Benches and Experimental Setups

Both laboratories utilized specially designed, high pressure facilities for their studies, sharing a common goal. Studies at AFRL have focused mainly on non-reacting flows, at a physical scale much smaller than the DLR non-reacting flow studies. Studies at DLR have also included reacting flows. Details of each facility can be found in the respective authors' previous publications, many of which are listed in the extensive references provided at the end of this paper (Branam and Mayer (2003), Chehroudi et al (1999-2004), Davis and Chehroudi (2004), Decker et al (1998), Mayer et al (1996-2003), Oschwald et al (1999-2002)). However, adequate information regarding the facility, injector geometries, and diagnostics used is necessary in order to better understand the results presented here and to make this paper reasonably self-sufficient and complete. Therefore a brief description of the facilities is given next.

2.1 AFRL test bench

Figure 6 shows a schematic diagram of the test bench at AFRL. The stainless steel chamber can withstand pressures and temperatures of up to 20 MPa and 473 K, respectively. It has two facing circular sapphire windows for optical diagnostics. Liquid N_2 is used to cool and/or liquefy the injectant passing through a cryogenic cooler (heat exchanger) prior to injection. The mass flow rate of the injectant is measured and regulated via a mass flowmeter and a precision micrometer valve. Back-illumination of the jet is accomplished with diffuse light flashes (0.8 µs duration). A model K2 Infinity long distance microscope is used with a high resolution (1280(H) x 1024(V) pixels in an 8.6(H)x6.9(V) mm actual sensing area with a pixel size of 6.7µm x 6.7 µm) CCD camera by the Cooke Corporation to form images of the injected jets. The injection for the single jet studies was through a sharp-edged 50 mm long stainless steel tube with a 1.59 mm (1/16") outer diameter and a 254 micron (0.010") inner diameter, resulting in a length-to-diameter ratio of 200. With the Reynolds number ranging from 25,000 to 70,000, the entrance length of 50 to 100 is needed for fully-developed turbulent flow (see Schlichting (1979)). The length is therefore long enough to ensure fully-developed turbulent pipe flow at the exit. For the coaxial injector, the cryogenic jet is injected through a sharp-edged stainless steel tube having a length L of 50 mm, and inner and outer diameters measuring $d_i = 0.508$ mm and $d_o = 1.59$ mm, respectively. The resulting L/d_i was 100, which is also sufficient to ensure fully-developed turbulent pipe flow at the exit plane. The Reynolds number in these studies ranged from 6,000 to 30,000. The outer tube had an inner diameter of 2.286 mm, forming a gaseous fluid annular passage of 0.348 mm in the radial direction. The bench is fully instrumented to measure pressure, temperature, and mass flow rate of the injected fluid. A specially designed piezo-siren by Hersh Acoustical Engineering, Inc., capable of producing sound pressure levels (SPL) of up to 180 dB in an impedance tube at its resonant frequencies (lying between 1000 to 8000 Hz) and at pressures up to 13 MPa was used with a circular-to-rectangular transition coupling to bring the acoustic waves into the interaction zone inside the chamber. A model 601B1 Kistler piezoelectric-type pressure transducer was used to measure the acoustic pressure variations inside the chamber at various pressures very near the jet location. The piezo-siren acoustic driver was able to generate between 161 to 171 db when coupled with the high-pressure chamber.

2.2 DLR cryo-injector test bench

The cryo-injector test bench at DLR is designed for experimental investigations of both single and coaxial jets at background pressures up to 6MPa. With N_2 as a model fluid, this pressure corresponds to a reduced pressure of 1.76. Quartz windows allow the application of qualitative visualization as well as quantitative optical diagnostic techniques (Oschwald and Schick 1999, Mayer et al. 2003). Two different injectors have been used. In early studies, the diameter of the LN2 tube was D=1.9 mm, with an L/D of 11.6. Later, in order to ensure fully developed pipe turbulence could be assumed as an initial condition, a new injector was designed with D=2.2 mm diameter and L/D=40. In coaxial injection experiments He as well as H_2 has

been used as a annular gaseous co-flow. H_2 is Raman active, and thus the gaseous component of choice for quantitative density measurements based on Raman scattering (Oschwald et al. 1999a).

2.3   DLR high pressure combustion test bench P8

The European test bench P8 is a French/German high-pressure test facility for research and technology investigations at combustion chamber conditions representative of modern cryogenic rocket engines. See Fig. 7. Propellant supply systems (LOX, LH2 and GH2) can provide pressures up to 360 bar at the test bench interface to the test specimen. Mass flow rates can be controlled between 200 g/s and 8 kg/s for LOX, 50 g/s and 1.5 kg/s for GH2, and 200 g/s and 3 kg/s for LH2, respectively. Further details regarding the test facility P8 can be found in the article of Haberzettl et al. (2000).

The model combustor "C" has been used in the hot fire tests and under supercritical pressures. The modular combustor is equipped with a single coaxial injector head. A module with optical access enables the application of non-intrusive optical diagnostic techniques at pressures as high as 9MPa. The windows are protected from the thermal loads by hydrogen film cooling at ambient temperature. The H_2 film cooling does not influence the flow or combustion processes at the near injector region, which is the primary area of interest for the studies presented here. As demonstrated during the latest tests, the combustion chamber can be operated with LOX and GH2 propellants for up to 300 sec continuously.

2.4   Diagnostic methods

The large density gradients associated with the cryogenic high pressure flows create a challenging environment for any quantitative optical diagnostics, as they result in large refractive index gradients. Even at supercritical pressures, when surface tension vanishes, the variation of the density field on small length scales is strong enough to cause reflection and refraction of the light beams. An initial evaluation of the effects of the distortion on imaging caused by the refraction showed that it can be neglected for the conditions discussed in this paper (see Oschwald and Schik (1999)). Both laboratories have found shadowgraphy and spontaneous Raman scattering to be the methods of choice for visualization and quantitative measurements.

2.4.1   Shadowgraphy

Although a qualitative, line-of-sight method, shadowgraphy has been shown to be an effective diagnostic tool to investigate single and coaxial jet injection. Due to the huge density gradients of the cryogenic supercritical fluids relative to the background gas, geometrical properties such as the spreading angle and the intact core length are accessible by this method regardless of whether the jet is subcritical or supercritical. Using a short time-exposure light source, more detailed information on features reflecting the interaction of the jet with its environment can be obtained. For instance, geometric properties of the jet surface area and characteristic length scales of the density variations in the mixing layer of the supercritical jet can be revealed.

When applying the shadowgraphy method in high pressure combustion, it is essential to gate the background light originating from the flame emission by short-exposure times. In the tests at the P8 bench at DLR, this has been accomplished by mechanical shutters.

2.4.2   Spontaneous Raman scattering

When a medium is irradiated, some fraction of the beam is scattered in all directions. If the medium contains particles of molecular dimension, a weak scattered radiation having the same wavelength is observed, called Rayleigh scattering. Raman, in 1928, discovered that the wavelength of a very small fraction of the scattered radiation by certain molecules shifted by an amount dependent upon the chemical structure of the molecules responsible for the scattering. The Raman spectra are obtained by irradiating a sample with a powerful visible monchromatic source. The scattered signal is usually observed at 90 degrees to the incident beam with a suitable visible-region detector or spectrometer, see Eckbreth (1996).

The scattered radiation is a very small percentage of the source, as a result detection and measurement is difficult except for the resonant Raman which is explained below. The scattered light is of three types, Stokes, anti-Stokes, and Rayleigh. The Rayleigh component has exactly the same frequency as the excitation source and is substantially more intense than either two. Stokes peak lines are found at wavelengths larger (lower energies) than the Rayleigh peak while anti-Stokes are at smaller (higher energies) than the wavelength of the source. It is critical to realize that the magnitude of the Raman shifts are independent of the wavelength of excitation source. Generally, the Stokes lines are more intense than the anti-Stokes and for this reason usually only this part of the spectrum is observed. It is also important to indicate that fluorescence can interfere with detection of the Stokes shifts but not with anti-Stoke shifts. This shift of the lines are specific to the scattering molecule and hence, in multi-component systems, Raman scattering allows the detection of each individual component. This property of the Raman diagnostics is an important advantage when compared to the visualization techniques such as shadowgraphy when analyzing mixing processes during a two-component coaxial injection.

The Raman signal strength at ambient conditions is proportional to the molecular number density. It is well known that at high densities, the Raman scattering cross-section becomes density dependent due to internal field effects. No reliable quantitative data are yet available for densities of cryogenic N_2 in the critical pressure region. In the experiments presented in this paper, densities have been calculated assuming a pressure independent cross section (Decker et al. 1998, Oschwald and Schik 1999). In the near injector region, the density gradients are extremely high for most of the injection conditions discussed here. When the excitation laser beam passes through this region, beam steering occurs, which leads to a blurred image in the Raman detection channel.

Two different optical setups were used by the DLR for Raman measurements. A continuous wave (CW) Ar-Ion laser operating at 488nm has been used by Oschwald and Schik (1999). A data acquisition time of 1s was necessary to achieve a sufficient signal-to-noise ratio. The use of a CW-laser practically prevents the formation of signal due to stimulated Raman scattering that may interfere with the spontaneous Raman signal.

Using a pulsed XeF excimer laser at 351 nm allows time-resolved single-pulse measurements to be performed (Decker et al., 1998, Mayer et al., 2003). The laser was operated with two independent laser tubes in a double oscillator configuration. The two laser tubes fired with a short delay to reduce the peak intensity of the laser and to increase the total pulse length to about 40 ns in order to avoid gas optical breakdown.

At AFRL, Chehroudi et al. (2000) used a frequency-doubled Nd:Yag pulsed laser (532 nm output wavelength) with a passive pulse stretcher designed to reduce the possibility of plasma formation. The original pulse was extended in time by dividing it into three major pulses, each being 10 ns in duration, but delayed in time by 8 ns and 16 ns. This resulted in a final pulse duration of about 26 ns. The scattered Raman signal was collected at 607 nm.

3 Single Jet Investigations

In a quest to understand liquid breakup mechanisms for injection at subcritical and supercritical pressures, researchers at DLR and AFRL began working with the simplest and perhaps the most popular and fundamental of all cases, that is, the injection of a single non-reacting round jet into a quiescent environment. The injection of the single jet was studied at various chamber pressures ranging from subcritical to supercritical, and included chamber pressures representative of those experienced in a typical cryogenic liquid rocket engine. For safety reasons it was preferred to simulate liquid oxygen with liquid nitrogen; early studies had confirmed that the injection behavior of these two fluids was similar as long as chemical reactions did not take place. To avoid complications introduced by mixture effects as discussed in section 1.2,

many of these studies involved injecting cryogenic liquid nitrogen into room temperature gaseous nitrogen. However, injection into other ambient gases was also investigated.

The results acquired by the groups were interpreted and analyzed both qualitatively and quantitatively. The purpose of this section of the paper is to present key findings by the groups and to highlight the conclusions confirmed independently by each laboratory regarding single jet injection.

3.1   Jet surface

3.1.1   Phenomenology at subcritical and supercritical pressures

Figure 8 shows representative images of cryogenic LN_2 jets injected into ambient temperature gaseous nitrogen at 300 K. The initial temperature of the jets was measured in separate experiments under identical flow conditions with a small thermocouple. Depending on the flow condition, the measured initial temperature varied from 99 K to 110 K. The bottom row of Fig. 8 shows a magnification of the image in the same column on the top row, to more clearly show the shear layer structure. Pressures in the figure are reported as reduced pressures, defined to be the chamber pressure divided by the critical pressure of nitrogen.

In column (a), where the chamber pressure is subcritical, the jet has a classical spray appearance. Consistent with the classical liquid jet breakup regimes described by Reitz and Bracco (1979), surface instabilities grow downstream from the injector, and very fine ligaments and drops are ejected from the jet. This has been confirmed to correspond to the second wind-induced liquid jet breakup regime described by Reitz and Bracco (1979).

Major structural and interfacial changes occur at about Pr = 1.03. Above this pressure, drops are no longer detected, and regular finger-like entities are observed at the interface. Rather than breaking up into droplets, the interface dissolves at different distances from the dense core. These structures are illustrated at P_r =1.22 in column (b) of Fig. 8. This change in the morphology of the mixing layer is evidently due to the combined effects of the reduction in the surface tension as the critical pressure is exceeded and disappearance of the enthalpy of vaporization because of this transition.

As chamber pressure is further increased, the length and thickness of the dense core decreases, and the jet begins to appear to be similar to a turbulent gaseous jet injected into a gaseous environment. This is illustrated in Fig. 8, column (c). Any further droplet production, and consequently, any additional classical liquid atomization, are completely suppressed. These observations were confirmed both at AFRL and DLR; for example, see Mayer et al. (1996, 1998) and Chehroudi, et. al. (2002). As mentioned above, similar results were found when injecting liquid oxygen.

Because of the large density variations in the chamber, it was of interest to establish whether the evolution of the jet within the region of measurement is affected by the buoyancy forces. Therefore, Froude number values were calculated for the AFRL facility at each condition. As an example, Chehroudi et al. (1999, 2002) showed that for their experiments the Froude number ranges from 42,000 to 110,000. Chen and Rodi (1980) suggested that the flow is momentum dominated when a defined length scale x_b is less than 0.53, while Papanicolaou and List (1988) suggested $x_b < 1$. The length scale is given by $x_b = Fr^{-1/2}(\boldsymbol{r}/\boldsymbol{r}_\infty)^{-1/4}(x/d)$, where x is the axial distance, d is the initial jet diameter, $\boldsymbol{r}$ and $\boldsymbol{r}_\infty$ are the jet and ambient densities, respectively. The Froude number is defined as $Fr \equiv \boldsymbol{r}U^2/gd|\boldsymbol{r}_\infty - \boldsymbol{r}|$ where U is the velocity difference, and g is the gravitational acceleration. Considering the more conservative estimate by Chen and Rodi (1980), the jet used by them is momentum dominated for distances less than 30 to 40 mm from the injector exit. Pictures presented in Fig. 8 cover up to about 5.5 mm (axial dis-

tance/diameter ratio of 21.6) from the injector, and hence buoyancy effects can be ignored in favor of inertial forces. This conclusion applies to all of the quantitative measurements performed at AFRL.

3.1.2 Length scale analysis

Disintegration of a single LN_2 jet without an annular co-flow gas has been investigated at DLR at ambient pressures of 4MPa and 6MPa, corresponding to a reduced pressure of 1.17 and 1.76 respectively. The initial injection temperature of the nitrogen was near the critical temperature and it was injected into an N_2 environment at a temperature of 298K. Branam and Mayer (2003) provided a measure of the length scales by analyzing the images taken through the shadowgraphy method and named it the "visible length scale." They isolated the intensity values of any two arbitrarily selected pixels located at a certain distance for 30 to 60 images and then formed the two-point correlation coefficient of these two sets of intensity information. Then, by changing the distance of one of these pixels with respect to the other fixed pixel, they were able to construct a correlation coefficient plot from which a "visible" length scale is calculated. The length scale can be determined through an integration operation, similar to the integral length scale, or by selecting the pixel-to-pixel separation at the 50% correlation value. The latter approach was selected for this particular analysis due to speed and ease of implementation, accepting a certain level of inaccuracy.

Both axial and radial length scales were determined in this manner. Figure 9 shows a typical result of the geometrically-averaged length scale (average of radial and axial length scales) measured at an x/D of 10 as a function of the radial position. Results from a k-ε computational method are also shown (see section 3.3.2). This suggests that the visible length scale is comparable in magnitude to the Taylor length scale as determined by the computational method.

The ratio of the axial to the radial length scales expresses whether the visible structures are spherical or more ellipsoidal. Both length scales are shown in Fig. 10 for an injection temperature of 123 K; i.e., injection of N_2 at a high density. In the near injector region, the axial length scales are much larger than the radial ones. Further downstream the visible structures become more circular in shape. At a higher injection temperature (132 K), the asymmetry between the L_{rad} and L_{ax} is not as pronounced as that seen under lower temperature conditions (123 K).

3.1.3 Fractal analysis

Fractals are intimately connected to the concept of self-similarity (see Mandelbrot (1983)). In essence, a similarity transformation involves one or a combination of multiplication by a scale factor, pure translation, and pure rotation. Under such a transformation a geometrical object stays similar to the original or to a preceding stage if repetitively applied. Self-similarity, however, in a strict sense means that if one chooses any point of a geometrical object and locally magnifies, it will look similar to the "whole" object. In nature, however, self-similarity is confined between two sizes (or scales) referred to as inner (the smallest size) and outer cut-offs (the largest size).

The fractal dimension of any curve is between 1 and 2. The more wrinkled and space-filling the curve, the larger the value of the fractal dimension. Natural curves, such as the outline of a cauliflower, are self-similar only to within a narrow range of scales. The objective here is to measure the fractal dimension of the interface of the jets injected into the chamber to see if any pattern is uncovered.

The fractal dimension of jets at various pressures ranging from subcritical to supercritical was calculated and compared to results of other researchers. Reference results were taken from Sreenivasan and Meneveau (1986) who measured the fractal dimensions of a variety of turbulent gaseous jets, mixing layers and boundary layers. These results indicate a fractal dimension between 1.33 and 1.38. In addition, the fractal dimensions of a turbulent water jet (Dimotakis et al. (1986)) and of a liquid jet in the second wind-induced atomization regime (Taylor and Hoyt (1983)) were computed from high-resolution scanned images.

The fractal dimensions from the above reference cases are shown as horizontal lines in Fig. 11. Overlaid on top of these lines are discrete points indicating the fractal dimension of LN2 jets injected into GN_2 at various chamber pressures. At supercritical chamber pressures, the fractal dimension approaches a value similar to gaseous turbulent jets and mixing layers. As the chamber pressure is decreased, the fractal dimension also decreases. Below P_r=0.8, the fractal dimension rapidly reduces to a value approximately equal to that of a liquid spray in the second wind-induced liquid jet breakup regime.

A more thorough discussion of the above results is found in Chehroudi and Talley (2004). The key conclusion here is that the results from fractal analysis complement and extend the imaging data. At supercritical pressures, jets have a fractal dimension similar to turbulent gas jets, and at subcritical pressures, cryogenic jets have a fractal dimension similar to liquid sprays. The transition occurs at about the same pressure as the transition in visual appearance and growth rate.

3.2 Jet decay

3.2.1 Visualization of jet core length

According to Abramovich (1963), the length of the potential core in isothermal uniform density axisymmetric and two-dimensional jets is estimated to be about 6 to 10 injector diameters; whereas for non-isothermal cold jets injected into hot environments, it can reach up to about 25 injector diameters depending on jet temperature.

Also, according to Chehroudi et al. (1985) the intact core length of the liquid sprays similar to the ones used in diesel engines is given by $Cd_j(\rho_l/\rho_g)^{1/2}$ where ρ_l and ρ_g are liquid injectant and chamber gas densities respectively, "d_j" is an effective jet exit diameter and C is a constant between 3.3 to 11. This translates to an intact core length between 33 to 110 injector diameters for the chamber-to-injectant density ratio of 0.01 and between 16.5 to 55 diameters for the chamber-to-injectant density ratio of 0.04. These results are presented in Fig. 12 (a) and (b) for better comparison with our current data.

Note that the classical two-stream mixing layer starts from the injector exit to approximately the end of the potential core (or intact core) of the jet. Assuming that the jet dark-core seen in images plays the same role as the intact core or potential core, Fig. 12(a) indicates that growth rate data (presented next) taken by Chehroudi et al. (2002) is from the corresponding and appropriate initial region to ensure existence of a classical mixing layer. It is only then that a valid comparison can be made between these results and the two-stream mixing layers available in the literature.

A complementary result by the DLR researchers is shown in Fig. 12 (b). These results were determined through a log-log plot of the centerline intensity measured by Raman scattering to distinguish different flow regions. Note that the horizontal axis for Fig. 12(a) and (b) are the inverse of each other. The DLR data are at or below the lower bound of the Chehroudi et al. (1985) model (i.e., solid curves in Fig. 12(b)) which was proposed based on the liquid spray data in various atomization regimes. For chamber-to-injectant density ratios of less than 0.1 in Fig. 12 (a) (or injectant-to-chamber ratio of greater than 10 in Fig. 12 (b)) it appears that the Chehroudi et al. experimental data shown in Fig. 12 (a) is larger by about a factor of 1.5 to 2 compared with the "correlation" data of Branam and Mayer (2003) in Fig. 12(b).

The core length measurements above are currently a point of disagreement between the two laboratories which needs to be investigated further. Considering that the raw data used by the two groups are from two different measurement methodologies (Raman versus shadowgraphy), however, such a result is perhaps not unexpected. In fact, Chehroudi et al. (2000) have also shown such differences when Raman and shadowgraphs were used in the context of growth rate measurements. However, improved techniques with more precise measurements are necessary in order to accurately assess this quantity. This is currently being investigated at AFRL.

3.2.2 Mapping of the density and temperature fields

The main purpose of using Raman scattering measurements was to provide quantitative information and to map out the jet density field. Using this information, temperatures can also be calculated assuming application of a suitable equation of state. Typically, results such as radial density profiles are presented in an appropriately normalized fashion. In addition to these density profiles, it should be apparent that the growth rate (or spreading angle) of the jet can also be extracted from these data. Growth rate data from these measurements are discussed in section 3.2.3 of this paper. Here the centerline density/temperature profiles as a function of the axial distance from the injector exit plane and the self-similarity assessment are discussed.

The test conditions were chosen in order to assess the influence of the thermodynamic state of the injected cryogenic N_2 on the jet disintegration process. A well known anomaly at the critical point is the singularity of the specific heat at the critical point, as mentioned earlier. Above the critical pressure, the specific heat is finite but exhibits a maximum at a particular temperature (see Fig. 4). At this same point, the thermal diffusivity exhibits a minimum. Three test cases were investigated as shown in Fig. 13 (a). In test case A, the initial injection temperature is both above the critical temperature and above the temperature where the specific heat is a maximum, whereas for test cases B and C the initial injection temperatures are both below the critical temperature and the temperature where the specific heat is a maximum.

Figures 13 (b) and (c) show normalized centerline profiles of the density and temperature acquired by Oschwald and Schick (1999) at a chamber pressure of 4 MPa (near the critical pressure of nitrogen). Note that the density decay becomes slower as the initial injection temperature is decreased. The temperature profile, however, stays flat for up to a normalized distance (x/D) of about 25 to 30. As pointed out by Oschwald and Micci (2002), the development of the centerline temperature reflects the thermophysical properties of the nitrogen, specific to the region where the specific heat reaches a maximum. For initial injection temperatures below the temperature where the specific heat reaches a maximum, as the jet heats up, the fluid has to pass a state with a maximum specific heat. It can reach a value where a large amount of heat can be stored without any noticeable increase in temperature. It appears that the maximum specific heat line in a supercritical fluid results a behavior similar to a liquid at its boiling point. That is, heat transfer to the nitrogen does not increase its temperature but merely expands the fluid (i.e., increases its specific volume). It is also for this reason that the dashed curves in Figs 5 and 13 (a) are referred to as "pseudo boiling lines." Note that the density of the fluid varies strongly with temperature in this zone. At 6MPa (P_r=1.76, data not shown), the maximum of the specific heat is much less pronounced and the effects of the pseudo-boiling line is not as distinct as those seen under chamber pressure of 4 MPa. As shown by Oschwald and Schik (1999) however, far downstream, it was observed that the temperature of the disintegrating and mixing supercritical fluid jet approaches a value representative of a fully-mixed jet, but at a slower pace than that for the jet density.

The self-similarity of the density field has also been investigated and the results are presented in Fig. 14. According to Wygnanski and Fiedler (1970), a fully self-preserved velocity field of a turbulent air jet should be observed at an x/D of greater than 40 when the Reynolds number is near 100,000. So et al. (1990) reported self-preservation for x/D values larger than about 20 in a binary gas jet at Re=4300. Although it appears that some inconsistencies exist in these criteria, one can see that for the near critical and supercritical pressures, the density radial profile approaches the similarity model curve in Fig. 14(a), with the disagreement being the largest at subcritical pressures where the model is the least applicable. Results published by Oschwald and Schick (1999) also indicate similarity-type profiles for x/D values greater than about 10. See examples of the two radial profiles of density from their work shown in Fig. 14(b).

3.2.3 Jet spreading angles

Measurements and estimations of the growth rate of a jet has been a subject of intense research because it provides a primary measure of mixing and development of the jet. Chehroudi et al. (1999) were the first to extract quantitative measurements of this physical parameter from the images taken of a cryogenic N_2 jet

injected into GN_2 under both subcritical and supercritical pressures. These measurements led to important conclusions regarding the character of the growth rate and the behavior of the jet under such conditions.

The spreading angle or growth rate is measured from a field of view within 5.5 mm from the injector exit plane (distance-to-diameter ratio of up to 21.6) and are inertially dominated as discussed in section 3.1.1. Results presented in Fig. 15 were also taken from the corresponding and appropriate initial region to ensure existence of a classical mixing layer. The initial jet spreading angle or its growth rate is measured for all the acquired images, and results along with those of others are presented in Fig. 15. Of importance in this figure is the justification for the selection of the data sets and the nature of their measurements by other researchers. They are elaborated in sufficient detail in earlier papers; in order to gain a deeper appreciation of these selections see particularly Chehroudi et al. (2002). Therefore, they are only mentioned here in brief as needed.

Since the jets investigated here exhibit both liquid-like and gas-like appearances, depending on pressure, appropriate comparisons for both liquid sprays and gas jets are presented in Fig. 15. The simplest is the prediction of the linear growth or constant spreading angle for the turbulent incompressible submerged jet using the mixing length concept. Following Abramovich (1963), a semi-empirical equation is used that attempts to incorporate the effects of density variations by an introduction of a characteristic velocity (see Chehroudi et al. (2002)).

Brown and Roshko (1974) measured spreading angles for a subsonic, two-dimensional, incompressible, turbulent mixing layer in which helium and nitrogen were used. Brown (1974) (for temporally growing mixing layer) and Papamoschou and Roshko (1988) proposed a theoretical equation for incompressible variable-density mixing layers. Finally, Dimotakis (1986) used the observation that, in general, the entrainment into the mixing layer from each stream is not the same and, in a system moving with a convection velocity, offered a geometrical argument to derive an equation for two-dimensional incompressible variable-density mixing layers. Predictions from all of these models are plotted in Fig. 15. Results by Richards and Pitts (1993) for variable-density jets are also noteworthy and have been taken into consideration by both groups.

Conversion of the two-dimensional mixing layer data for comparison with our data is justified because, according to both Brown and Roshko (1974) and Abramovich (1963), two-dimensional mixing layers are found to be fairly well approximated by the initial mixing region of axisymmetric jets. For this reason all angle measurements by Chehroudi et al. (2002) were made using only the information within the first 5.5 mm from the injector exit plane. Because both liquid-like and gas-like visual jet behaviors are observed, the growth rate for the liquid sprays produced from single-hole nozzles, typical of the ones used in diesel engines, are also shown in this figure. Figure 15 covers a density ratio of four orders of magnitude, a unique and new plot in its own right. To some extent, and for comparable cases, disagreements in this figure can be attributed to differences in the definition of the mixing layer thicknesses and the adopted measurement methods. For detailed discussion of this figure, see Chehroudi et al. (1999, 2002).

The important point shown in Chehroudi et al. (2002) is that for a range of density ratios in which images show gas-jet like appearance, the experimental data agrees well with the proposed theoretical equation by Dimotakis (1986) and closely follows the trend of the Brown/Papamoschou and Roshko equation as shown in Fig. 15. This can be taken as an important quantitative evidence that at supercritical pressures, the injected jets visually behave like a gas. Chehroudi's work was the first time such quantitative evidence had been developed. The fractal results discussed in section 3.1.3 later added additional evidence for the hypothesis.

It is worth mentioning that above the critical point, there is a marked disagreement in both magnitude and slope between the liquid sprays (at a comparable length-to-diameter ratio of 85) and Chehroudi et al. data (see Fig. 15). Approaching the critical point, the jet appears to go through initial phases of the liquid at-

11

omization process, as shown in Fig. 8; however, the cascade of events typical of the liquid jet atomization and break-up does not take place once the critical point is passed. The reason is that, although the jet shows the second wind-induced breakup features similar to liquid jets, it fails to reach a full atomization state as chamber pressure (actually, density) is raised. This is because the pressure approaches the critical pressure, and consequently both surface tension and heat of vaporization are reduced to near-zero values. Transition into the full liquid atomization regime is therefore inhibited and hence no agreement is seen between the liquid sprays and our jet beyond such point

Initially, the growth rate measurements by Chehroudi et al. using results acquired during the Raman scattering work did not provide the same jet thickness values as those determined by the shadowgraphy. Apparently, as discussed by Brown and Roshko (1974), different thickness definitions exist, and one can explore their relationship. Similar attempts showed that within the distances investigated, twice the full width half maximum (FWHM) of the Raman intensity radial profiles was equivalent to the thickness values measured through photography. Realization of this relationship was very critical to combine the results from two different methodologies. Figure 16 shows the growth rate measured using the Raman data in contrast to those determined by shadowgraph images.

These results were subsequently confirmed and extended by DLR researchers through a similar measurement technique. For example, Oschwald and Micci (2002) showed that when twice the FWHM of the Raman radial intensity profiles are used for x/D values within 15 and 32, a good agreement exists between the results from the two laboratories (see the case designated as "p=0.36" in Fig. 17, where "p" is the exponent of the curve fitted through the data). However, the twice FWHM criterion did not agree with shadowgraphs as well for x/D < 15 in the study of Oschwald and Micci (2002) (see the case identified as "p=1.0" in Fig. 17).

Results from Oschwald and Micci (2002) are plotted in a different form in Fig. 18, as tangent of the spreading angle as a function of density ratio. Again it is shown that the twice FWHM criterion sometimes does and sometimes does not predict the shadowgraph data.

Within the x/D values which both laboratories studied in common, both laboratories confirmed the twice FWHM criterion for those values. DLR measured a larger range of axial distances, and found that the criterion was not universal at extended ranges. AFRL has not yet attempted to duplicate these extended measurements, but care in interpreting the results would in any case be warranted. Even if a different trend were to be observed, it is possible that the results of the two laboratories would still be fully consistent with each other. There are several reasons why different trends might be observed. It has to be noted that shadowgraphy and Raman scattering measure different physical properties. The Raman signal is taken to be proportional to density whereas shadowgraphy is sensitive to the gradients of the density distribution. Thus a unique relationship between the results measured by the two methods may only be valid for specific configurations. Recall that the data discussed above were obtained from injectors with different L/D ratios. Another potential cause of problems is errors in attempting to perform Raman measurements close to the injector inlet where density variations and thus index of refraction variations can be very large.

3.2.4 Jet disintegration under the influence of an external acoustic field

Overwhelming evidence gathered by investigations in the past have attributed combustion instability to a complex interaction of the external acoustic field with the fuel injection processes, thereby leading to incidences of instability in rocket engines. Also, Oefelein and Yang (1993) indicated that the near-injector processes in the thrust chamber are generally more sensitive to velocity fluctuations parallel to the injector face than normal to it. For this and other reasons, controlled studies have been conducted in the past probing into the effects of acoustic waves on the gaseous and liquid jets from a variety of injector designs.

Chehroudi and Talley (2002a) used a unique piezo-siren design capable of generating sound waves with a sound power level (SPL) of up to 180 dB. This was used at three chamber pressure conditions of 1.46,

2.48, and 4.86 MPa (reduced pressures of 0.43, 0.73, and 1.43, respectively). The assembly, consisting of an acoustic driver and a high-pressure chamber, forms a cavity that resonates at several frequencies, the strongest being at 2700 and 4800 Hz. They injected LN_2 into GN_2 at room temperature under sub- and supercritical pressures. Three different flow rates were considered, and the nature of the aforementioned interaction was documented via a high-speed imaging system using a CCD camera.

Figure 19 shows some sample results from this study. It appears that the acoustic field constricts the jet in the wave propagation direction and stretches the jet in the direction perpendicular to the propagation. Chehroudi and Talley (2002) found that the impact of the acoustic waves on the jet structure is strong at subcritical pressures, strongest at near-critical pressures, and weakest at supercritical pressures. They also observed that the interaction was the strongest at low injectant flow rates. The weak effect at supercritical pressures suggests that the mechanisms governing the coupling between acoustic waves and jets may be significantly different for supercritical jets than for subcritical jets.

3.3 Modeling and simulation of single jet injection at high pressure

3.3.1 Phenomenological model of the jet growth rate
Using the experimental data collected on the growth of a cryogenic jet, a phenomenological model for the growth rate has been developed. Complete details on the development of this equation are to be found in Chehroudi et al. (1999a). The physical reasoning motivating the proposed model equation is outlined below.

It was noticed that previous expressions for the growth rate of liquid sprays and of turbulent jets have a remarkably similar form. Reitz and Bracco (1979) proposed that the growth rate of an isothermal steady liquid spray could be expressed as,

$$q \approx 0.27[0 + (r_g / r_l)^{0.5}].$$

The first term in the bracket is the number zero to contrast with other equations discussed next. Similarly, Papamoschou and Roshko (1988) suggested the following form for incompressible, but variable-density, turbulent gaseous jets:

$$q = 0.212[1 + (r_g / r_l)^{0.5}].$$

The similarity in the form of these equations suggests a potential for a linkage between the two cases. Imagine a jet that is being injected into a subcritical pressure environment similar to the ones shown in Fig. 8. Clearly there are drops and ligaments, testifying to the existence of a surface tension. Also, evidence of a phase change is seen. Hence, one appropriate characteristic time of the problem (at subcritical, $P_r<1$) is the "bulge" formation/separation time (τ_b) on the interface of the turbulent liquid jet. This time characterizes the formation and separation event of bulges from the liquid jet producing isolated ligaments and drops. Tseng et al. (1995) suggests that this time is equal to $(\rho_l L^3/\sigma)^{1/2}$ for the primary breakup in turbulent liquid jets, where ρ_l, L, and σ are liquid density, characteristic dimensions of turbulent eddies, and surface tension, respectively. The second relevant characteristic time (for subcritical jets) is the gasification time (τ_g). Here, an estimate of this time is calculated through the so-called D-squared law for drops to be equal to D^2/K where D and K are drop diameter and vaporization constant, respectively. In addition, we also propose the following hypothesis. If the aforementioned characteristic times (calculated for appropriate length scales) are nearly equal in magnitude, then the interface bulges are not able to separate as unattached entities from the jet interface to form ligaments and drops, because they are gasified as fast as they desire to be detached. Here, this is defined as the onset of the gas-jet like behavior. Therefore, the transition between liquid-like and gas-like behavior would be governed by finding the point at which these time scales are approximately equal. This picture is also suggested by the comb-like structures seen in Fig. 8(b).

13

Using the above physical models, an equation was proposed for the N_2/N_2 system as

$$q = 0.27[(t_b/(t_b + t_g) + (r_g/r_l)^{0.5}].$$

In the limit, when $\tau_g >> \tau_b$ and $\tau_g \to \infty$, this equation collapses to the isothermal liquid spray case. This equation agrees well with the current data at subcritical pressures for $t_b/(t_b + t_g) < 0.5$. A constant value of 0.5 was used to predict the spreading rate for higher pressures, including supercritical pressures.

For injection of N_2 into N_2, the characteristic time ratio, $t_b/(t_b + t_g)$, was calculated from the experimental measurements of bulge and droplet sizes and calculations of the relevant properties. For N_2 injection into other gases, however, reliable information about the mixture properties at the interface, particularly the surface tension, prevents such a calculation from being performed. To model these cases, it is hypothesized that the characteristic time ratio is a dominant function of the density ratio; i.e., $t_b/(t_b + t_g) = F(r_g/r_l)$. Brown and Roshko (1974) indicate that this hypothesis is reasonable, because at low Mach numbers there is no distinction between mixing layers where the two streams have different molecular weights, temperatures, or compressibility effects. Measurements and calculations of $t_b/(t_b + t_g)$ provides the shape of the function F for the N_2/N_2 system and is provided as a plot in Chehroudi et al. (1999a). A curve fit of that plot gives

$$F(r_g/r_l) = 5.325\ (r_g/r_l) + 0.0288 \qquad when \qquad r_g/r_l < 0.0885$$
$$= 0.5 \qquad when \qquad r_g/r_l \geq 0.0885$$

It was found that the same function, F, calculated from measurements of the N_2/N_2 system could be made to work for other cases, provided that a case-dependant transformation was made to the density ratio at which F is evaluated. The final form of the equation thus arrived at is

$$q = 0.27[F(x(r_g/r_l)) + (r_g/r_l)^{0.5}],$$

where, x=1.0 for N_2-into-N_2, x=0.2 for N_2-into-He, and x=1.2 for N_2-into-Ar.

In other words, the same functional form of the characteristic time ratio, $t_b/(t_b + t_g) = F(?_g/?_l)$, for the N_2-into-N_2 case is used but with a density-ratio coordinate transformation. The quality of the agreement with experimental data is demonstrated in Fig. 20. Hence there are no major changes in the form of the proposed model equation, even for an extreme arrangement such as injection of N_2 into He. However, an observation is made here. The factor x=0.2 in the N_2-into-He case is comparable to the molecular weight ratio of He to N_2 of 0.14, while the factor x=1.2 in the N_2-into-Ar case is comparable to the molecular weight ratio of 1.42. This also suggests the dominant effect of the density ratio parameter between the cases.

3.3.2   Numerical simulation of injection under supercritical pressures (LN2 into GN2)

Supercritical injection has been simulated using a commercial CFD program. The intention was to use the simulations as an engineering design tool. However, the reliability of the results produced by the program needs to be evaluated by a comparison with the experimental data. Using the CFD-ACE software package, simulation of this multi-physical problem appeared as a straightforward computational approach. Details of the simulation technique are given by Mayer and et al. (2001). Real gas nitrogen properties have been used and the computational model can capture the weakly compressible effects.

The software package takes into account turbulent heat transfer by use of a turbulent Prandtl number. The effective coefficient of thermal conductivity K_{eff} is modeled according to

$$K_{eff} = K + \frac{n_T r c_p}{Pr_T}$$

where $\Pr_T = \dfrac{\boldsymbol{n}_T}{\boldsymbol{k}/\boldsymbol{r}c_p}$ is the turbulent Prandtl number. A constant value of $\Pr_T$=1.0 proved to be consistent with the experimental findings.

The boundary conditions for this model are very important and extremely sensitive to the values of temperature. Measured mass flow, temperature, and pressure determine the injector exit conditions. From measurements of these quantities, initial inlet velocity, turbulent kinetic energy (k) and rate of dissipation (ε) are calculated and considered as the inputs to the model.

The simulation predicts a transition from a top-hat (liquid-like jet) shape to a fully-developed (gas-like jet) behavior as shown in Fig. 21. The normalized density $r^* \equiv (\boldsymbol{r}_{\text{jet}} - \boldsymbol{r}_{\text{ambient}})/(\boldsymbol{r}_{\text{jet}} - \boldsymbol{r}_{\text{ambient}})_{\text{max}}$ is plotted as a function of the radial distance, normalized by $r_{1/2}$, the value at which ρ^*=1/2. Note that for x/D>10, all simulated density fields $\rho^*(r/r_{1/2})$ fall relatively close together, indicating a nearly self-similar behavior. The experimental data appears to confirm this, but the uncertainty in the Raman data is not sufficiently resolved to confirm it. For the axial velocity $u^* \equiv (u_{\text{jet}} - u_{\text{ambient}})/(u_{\text{jet}} - u_{\text{ambient}})_{\text{max}}$ profiles, the transition to the self-similarity behavior is seen to occur at a similar normalized distances as the density profiles, see Fig. 22. Note that, all radial profiles of $u^*(r/r_{1/2})$ are rather identical for x/D>10.

For all the test cases, the simulation results predicted the existence of a potential core. Figure 23 shows the normalized centerline density as a function of axial distance from the injector for an initial injection temperature of 133K, which is above the pseudo-boiling line. The simulation indicates a potential core length of about x/D=7.6. The potential core length increased as the initial injection temperature decreased. For example, in Fig. 24, a cryogenic nitrogen jet with an injection temperature of 120 K, falling below the pseudo-boiling line, shows a simulated potential core length of about x/D=9. The experimental results derived from the Raman data show this effect more dramatically. For the 133 K injection temperature, the normalized potential core length is shorter than about x/D=5. For the 120 K injection temperature case, the measured centerline densities match the computer simulation data quite well, see Fig. 24.

At a distant of x/D = 150, the density falls off quickly toward the chamber value, suggesting that the jet has almost completely dissipated. The calculations showed that this location in the chamber was at the far edge of a recirculation zone established to transfer mass back toward the injector exit area. This is the mass entrained in the jet flow from the chamber environment.

4 Coaxial Jet Investigations

4.1 Non-reactive coaxial jet atomization

4.1.1 Visualization of coaxial LN2/He-injection

The influence of the ambient pressure on the atomization phenomena from subcritical to supercritical pressures has been experimentally studied for coaxial LN2/He injection. Telaar et al. (2000) used a coaxial injector with an inner diameter of d_{LN2} = 1.9 mm for the cryogenic nitrogen flow and an annular slit width of 0.2 mm with an outer diameter of 2.8 mm for helium. Two examples of the flow visualization by shadowgraphy near the injector region are shown in Fig. 25. The changes in the atomization mechanism at a reduced surface tension is quite evident. At the low chamber pressure of 1 MPa in Fig. 25A, a liquid spray is formed, whereas at the supercritical pressure of 6 MPa in Fig. 25B, a gas-like turbulent mixing of the dense and light fluids is seen. At 6 MPa in Fig. 25B, the initial temperature of the center LN2 jet was 97 K, whereas the critical mixing temperature of He/N2 mixtures at this pressure is 125.7K. Thus, in the mixing layer between the LN_2 and He, transcritical zones may exist. The visual boundary of the LN_2 jet as shown in Fig. 25 is assumed to be the layer at which the temperature reaches the critical mixing temperature. The influence of the surface tension forces as compared to the shear forces appears to be negligible.

4.1.2 Density measurements in a coaxial LN2/GH2-jet

In previous sections, the potential of the spontaneous Raman scattering as a diagnostic tool for quantitative density measurements was demonstrated in the context of injecting a single LN2 jet into the nitrogen gas. In a mixture of N_2 and H_2, however, the Raman signals of the N_2 and H_2 are generated at two different wavelengths. Thus, using an appropriate filtering technique, the signals from both species can be analyzed independently and the partial densities of each species can be determined.

This diagnostic method has been used to investigate the atomization and mixing of coaxial LN_2/H_2 injection at pressures which are supercritical with respect to critical pressure of pure nitrogen (Oschwald et al. (1999a)). The test matrix is listed in Table 3 and in Fig. 13a. During all the tests, the fluids were injected into a flow channel filled with N_2 at near atmospheric temperature at a pressure of 4MPa (P/P_{crit}=1.17). Plots for coaxial LN_2/H_2 injection are shown in Fig. 26(b), as contrasted with a single jet case shown in Fig. 26(a). The decrease of the measured densities at large positive r/D values is due to the refraction of the laser beam experienced as a result of the density gradients existing at the H_2/LN_2 interface. Similar radial profiles have been obtained for a range of axial distances from the injector. From these data, the two-dimensional species distribution can be reconstructed. For the test case designated by the symbol D4, such a distribution for the H_2 is shown in Fig. 27.

The maximum of the radial density distribution at each axial distance has been plotted as functions of the normalized distance (x/D) from the injector in Figs. 28, 29, and 30. This is used as a measure of the evolution of the injection process for the LN_2 jet downstream of the injector, as well as the mixing between the H_2 and N_2 species. Compared to the test case without the co-flow (Fig. 13b), it appears that the existence of the H_2 co-flow lowers the measured nitrogen density much faster from its initial injection value of (r_{INJ}) to a plateau (r_∞). The x/D value at which this plateau occurs represents a complete mixing of the jet with its background gas. The axial distance ($x_{1/2}$) at which the nitrogen density falls by 50% ($r(x_{1/2}) = r_\infty + 0.5(r_{INJ} - r_\infty)$) is determined and listed in Table 4. In comparing test case A4 (no co-flow, Fig 13b) with test case D4 (with co-flow, Fig. 28), it can be seen that the co-flow of H_2 increases the mixing efficiency of the injector. Also, in comparing test case D4 (T_{N2}=140K, Fig. 28), where the initial temperature is above the pseudo-boiling temperature, with test cases E4 (T_{N2}=118K; Fig. 29) and F4 (T_{N2}=118K; Fig. 29), it can be seen a jet initially above the pseudo-boiling temperature has a shorter decay length than a jet with an injection temperature initially below it. In both cases, the injected N_2 is at a supercritical pressure. However, nitrogen above the pseudo-boiling temperature has a gas-like density, whereas N_2 below this temperature has a much higher, liquid-like density. Thus the jet has more inertia to resist the shear forces from the annular H_2 jet. The effect of higher H_2 velocity was found not to be as pronounced as this effect of the initial N_2 density. This is seen when comparing the decay-lengths of the test cases E4 (v_{H2} = 120 m/s) and F4 (v_{H2} = 60 m/s) in Figs. 29 and 30, respectively.

Although a decrease in the density of H_2 with axial distance might reasonably have been expected, the Raman measurements in Figs. 28 and 20 show that the opposite trend can occur. This effect is significantly more pronounced for the test case of E4 (T_{N2}= 118 K) in Fig. 29 than that of D4 (T_{N2} = 140 K) in Fig. 28. The increase of the hydrogen density is therefore attributed to the net result of two effects: heat transfer from the hydrogen to the cryogenic nitrogen (cooling it down) and diffusion of the hydrogen into the dense nitrogen areas. In the near injector zone, the net effect is dominated by the heat transfer to the cryogenic N2, resulting in a decrease of the hydrogen temperature and consequently an increase in its density.

4.1.3 Coaxial LN2/GN2-injection under the influence of an external acoustic field

Cold flow studies of the interaction of acoustic waves with single jets have recently been extended to include coaxial injectors, and initial attempts made to understand how the results may relate to historical liquid rocket engine instability data. Preliminary results were reported by Chehroudi et al. (2003) and Davis and Chehroudi (2004). The observation that the interaction with acoustic waves tends to be stronger

at subcritical pressures than at supercritical pressures appears to remain generally true, although an influence of the mass flow ratio and initial temperature was also observed. Efforts continue to be underway to better understand how the various parameters control coupling mechanisms.

4.2 Hot fire tests: LOX/GH2-injection (DLR)

Thus far, injection and mixing have been demonstrated to be very different even in cold flow, depending on whether the pressure is subcritical or supercritical. However, heat release due to chemical reactions may also be expected to have a first order effect. Accordingly, combustion studies have been performed at DLR.

Shadowgraphs of the combustion a LOX/H_2 coaxial jet at subcritical and supercritical pressures is shown in Fig. 31, from Mayer and Tamura (1996). The chamber pressure in Fig. 31a was 1.5 MPa, well below the critical pressure of pure oxygen (5.04 MPa). The chamber pressure in Fig. 31b was 10 MPa, well above the critical pressure. In Fig. 31a, the shadowgraph shows that the LOX jet undergoes atomization with evidence of surface tension. A spray is formed having flow patterns similar to those visualized in cold flow studies. Ligaments are detached from the LOX jet surface, which then forms droplets which finally go through the evaporation process. The droplet number density was found to be much lower than the cold flow conditions, a fact that is due to the rapid vaporization of the small droplets in the burning spray.

At 10 MPa, the mixture may initially be below the critical mixing temperature. However, due to the convective transport of hot gases from the reaction zone to the O_2 jet surface, the local temperature will increase and the jet reaches a supercritical temperature. A shadowgraph of the O_2 jet at 10 MPa is shown in Fig. 31b. Droplets are no longer visible, and stringy or thread-like structures are seen attached to the O_2-jet which typically develop, grow, and rapidly dissolve without separation from the main jet. There is no evidence of surface tension. At this pressure, the flow is dominated by the turbulent gas-like mixing processes. The boundary between the dense, cryogenic O_2 core and the gaseous co-flow appears fuzzy with a smooth transition from the center of the jet to far radial distances, a contrast to the well-defined boundary between the liquid O_2 jet and the co-flow gas at 1.5 MPa seen in Fig. 31a.

Further downstream in Fig. 31b at 10 MPa, the visualization showed an oscillating but compact jet core, whereas at 1.5 MPa in Fig 31a, the jet has already disintegrated into ligaments and droplets. Magnified images of the region between 60-72mm downstream of the injector are shown in Fig. 32 for three chamber pressures. These demonstrate a remarkable difference in injection processes as a function of pressure. At 1.5 MPa (subcritical relative to pure oxygen), a spray of LOX droplets and ligaments can be seen. At 6 MPa and 10 MPa (supercritical relative to pure oxygen), the jet disintegrates into O_2 clumps of a size much larger than a typical liquid entity observed in the subcritical case.

5 Summary and Conclusions

Two independent laboratories have conducted studies of the injection of cryogenic liquids at subcritical and supercritical pressures, with application to liquid rocket engines. The results have been reviewed and compared here. In some cases, the findings of each laboratory corroborate each other, in other cases there are differences which need to be addressed, and in other cases, results have been obtained which the other laboratory has not attempted to verify. The conclusions to date can be summarized as follows.

For single round jets of cryogenic nitrogen injected into room temperature gaseous nitrogen, both laboratories have confirmed that the visual appearance of the jet undergoes a drastic change as the pressure is increased from a subcritical to a supercritical value. The subcritical jet has the appearance of a conventional spray, but the supercritical jet has a more gas-like appearance. Both laboratories have confirmed that the spreading rate of supercritical jets based on shadowgraph measurements is quantitatively the same as that predicted by theory for variable density gas mixing layers. Both laboratories have also compared

shadowgraph measurements with density profiles obtained from spontaneous Raman scattering. The Raman measurements were found to be most useful in supercritical jets, due to issues with stimulated and plasma emission in subcritical jets. Both laboratories have confirmed that the density profiles of supercritical jets approach self-similar shapes at about 10 diameters downstream. At axial distances which both laboratories have studied, both laboratories have confirmed that the spreading angles of supercritical jets measured using shadowgraphy correspond to the spreading angles measured using Raman scattering when the jet width using the latter is defined to be twice the full width half maximum (FWHM) distance of the measured density profiles. However, DLR explored a larger range of axial distances than AFRL, and found that the twice FWHM rule may not apply universally at all axial distances. AFRL has not yet attempted to independently confirm this finding. Both laboratories have also attempted to measure the length of the potential core, but with different diagnostic methods. The AFRL measurements were performed using shadowgraphy, and were found to be larger by a factor of 1.5 to 2 than the DLR measurements, which were performed using Raman scattering. The reason for the discrepancy needs to be further explored, but could be due to the different physical quantities measured by the two diagnostic methods.

DLR demonstrated a significant effect of the initial jet temperature, depending on whether this temperature is above or below the pseudo-boiling temperature, defined to be the temperature at a supercritical pressure where the specific heat reaches a maximum. Jets having an initial temperature below the pseudo-boiling temperature have to pass through this maximum in specific heat, where heat addition can result mostly in expansion with little increase in temperature, i.e., a pseudo-boiling process. The initial temperature of the jet can be preserved a considerable distance downstream. On the other hand, the temperature of jets having an initial temperature initially above the pseudo-boiling temperature decays monotonically from the injection point. DLR also measured length scales from shadowgraph images, and found that these visible scales correspond most closely to Taylor length scales. For initial temperatures close to the pseudo-boiling temperature, the axial length scales near the jet exit can be much longer than the radial scales. At higher initial temperatures, the disparity between the axial and radial length scales decreases. The disparity between the axial and radial length scales for all jets also decreases as a axial distance increases.

AFRL measured the fractal dimension of the jets, and found that the fractal dimension of subcritical jets approaches that of conventional sprays, while the fractal dimension of supercritical jets approaches that of gas jets. AFRL also studied cryogenic nitrogen jets injected into various gases other than nitrogen, and developed a semi-empirical model for their spreading rates. Finally, AFRL studied the effect of transverse acoustic waves on the jets, and found that the waves have a significant effect on subcritical jets, but significantly less effect on supercritical jets. Preliminary results for coaxial jets suggest that this general trend may continue to be true, although additional effects of mass flow ratio also seem to be evident.

For coaxial jets, AFRL has focused mainly on acoustic effects as described above. On the other hand, DLR has performed broader non-acoustic studies. In general, whether in cold flow or hot fire, these studies continue to confirm spray-like behaviour at subcritical pressures and gas-like behaviour at supercritical pressures. Raman studies were performed on N_2/H_2 jets, where N_2 and H_2 densities could be measured separately by detecting different wavelengths. It was found that the H_2 co-flow produced more efficient mixing than without co-flow. Initial temperatures above the pseudo-boiling temperature also produced more efficient mixing than initial temperatures below it. It was also found that the H_2 density can increase with downstream distance, due to cooling by the cold central jet.

In hot fire, the combustion of LOX/H_2 coaxial jets showed that the subcritical LOX breaks up into small ligaments and drops far downstream. In contrast, supercritical O_2 was found to break up into large clumps having typical dimensions much larger than corresponding subcritical entities.

6   Acknowledgements

18

References

Abramovich, G. N. (1963) *The Theory of Turbulent Jets*, MIT Press, Cambridge.

Branam, R. and Mayer, W. (2003) Characterization of cryogenic injection at supercritical pressure, *Journal of Propulsion and Power*, **19** (3), 342-355.

Brown, G. and Roshko, A. (1974) On density effects and large structure in turbulent mixing layers, *J. Fluid Mech.*, **64** (4), pp. 775-816.

Brown, G. (1974) The entrainment and large structure in turbulent mixing layers, *5th Australian Conference on Hydraulics and Fluid Mechanics*, pp. 352–359.

Chehroudi, B., Chen, S.-H., Bracco, F.V., Onuma, Y. (1985) On the intact core of full-cone sprays, *SAE Transaction Paper* 850126

Chehroudi, B., Talley, D., and Coy, E. (1999) Initial growth rate and visual characteristics of a round jet into a sub- to supercritical environment of relevance to rocket, gas turbine, and diesel engines, *AIAA* 99-0206, 37th AIAA Aerospace Science Meeting and Exhibit, Reno, NV, 11–14 January.

Chehroudi, B., Talley, D., and Coy, E. (1999a) Fractal geometry and growth rate changes of cryogenic jets near the critical point, *AIAA* 99-2489, 35th Joint Propulsion Conference, Los Angeles, CA

Chehroudi, B., Cohn, R., Talley, D., Badakhshan, A. (2000) Raman scattering measurements in the initial region of sub- and supercritical jets, *AIAA* 2000-3392, 36th Joint Propulsion Conference, Hunt sville, AL.

Chehroudi, B., Talley, D., and Coy, E. (2002) Visual Characteristics and Initial Growth Rates of Round Cryogenic Jets at Supercritical and Supercritical Pressures, *Physics of Fluids*, **14**, No. 2.

Chehroudi, B. and Talley, D. (2002a) Interaction of acoustic waves with a cryogenic nitrogen jet at sub- and supercritical pressures, *AIAA* 2002-0342, 40th Aerospace Sciences Meeting and Exhibit, Reno, NV

Chehroudi, B., Davis, D., and Talley, D. (2003) *Initial Results from a cryogenic coaxial injector in an acoustic field*, *AIAA* 2003-1339, 41st Aerospace Sciences Meeting and Exhibit, Reno, NV

Chehroudi, B. and Talley, D., (2004) Fractal Geometry of a Cryogenic Nitrogen Round Jet Injected into Sub- and Super-critical Conditions, Atomization and Sprays, vol. 14, pp. 81-91, 2004.

Chen, C. J. and Rodi, W. (1980) *Vertical Turbulent Buoyant Jets- A Review of Experimental Data*. Pergamon Press.

Davis, D. and Chehroudi, B. (2004). The Effects of Pressure and Acoustic Field on a Cryogenic Coaxial Jet, 42nd AIAA Aerospace Sciences Meeting and Exhibit, Paper No. AIAA-2004-1330, Reno, Nevada, January 5-8, 2004.

Decker, M., Schik, A., Meier, U.E., Stricker, W. (1998) Quantitative Raman imaging investigations of mixing phenomena in high-pressure cryogenic jets, *Applied Optics*, **37** (24), 5620-5627.

Delplanque, J.-P. and Sirignano, W.A. (1993) Numerical study of the transient vaporization of an oxygen droplet at sub- and supercritical conditions, *Int. J. Heat Mass Transfer*, **36**, pp. 303-314.

Dimotakis, P.E. (1986) Two-dimensional shear-layer entrainment, *AIAA Journal*, **21** (11) pp. 1791-1796

Eckbreth, A. (1996). *Laser Diagnostics for combustion, temperature, and species*, 2nd Edition, Combustion Science and Technology Book series, Vol. 3, Gordon and Breach Publishers.

Haberzettl, A., Gundel, D., Bahlmann, K., Oschwald, M,. Thomas, J.L., and Vuillermoz, P. (2000) European research and technology test bench P8 for high pressure liquid rocket propellants, *AIAA* 2000-3307, 36th Joint Propulsion Conference.

Macleod, D.B. (1923) Relation between surface tension and density, *Transactions of the Faraday Society*, **19**, 38.

Mandelbrot, B. B. (1983) *The Fractal Geometry of Nature*, W. H. Freeman and Company, San Francisco.

Mayer, W., and Tamura, H. (1996) Propellant injection in a liquid oxygen/gaseous hydrogen rocket engine, *Journal of Propulsion and Power*, **12** (6), pp. 1137-1147.

Mayer, W., Schik, A., Schweitzer, C., Schaffler, M. (1996a) Injection and mixing processes in high pressure LOX/GH2 rocket combustors, *AIAA Paper* No. 96-2620, 32nd AIAA/ASME/SAE/ASEE Joint Propulsion Conference & Exhibit, Lake Buena Vista, Florida.

Mayer, W., Schik, A., Vielle, B., Chaveau, C., Gökalp . I., and Talley, D. (1998) Atomization and Breakup of cryogenic propellants under high pressure subcritical and supercritical conditions, *Journal of Propulsion and Power*, **14** (5), pp. 835-842.

Mayer, W., Ivancic, A., Schik, A., Hornung, U. (1998a) Propellant atomization in LOX/GH2 rocket combustors, *AIAA Paper* No. 98-3685, 34th AIAA/ ASME/SAE/ASEE Joint Propulsion Conference & Exhibit, Cleveland, Ohio, 13-15 July.

Mayer, W., Telaar, J., Branam, R., Schneider, and G., Hussong, J. (2001) Characterization of Cryogenic Injection at Supercritical Pressure, *AIAA 2001-3275*, 37th Joint Propulsion Confrence

Mayer, W., Telaar, J., Branam, R., Schneider, and G., Hussong, J. (2003) Raman Measurements of cryogenic injection at supercritical pressure, *Heat and Mass Transfer*, **39**, 709-719.

Mayer, W., and Smith, J. (in press), Fundamentals of supercritical mixing and combustion of cryogenic propellants, *Rocket Engine Thrust Chambers*, AIAA Progress in Aeronautics and Astronautics

Nicoli, C., Haldenwang, P., Daou, J. (1996) Substitute mixtures for LOX droplet vaporization study, *Combustion Science and Technology*, **12**, pp. 55-74.

Oefelein J. C. and Yang, V. (1993) Comprehensive review of liquid propellant combustion instabilities in F-1 engines, *Journal of Propulsion and Power*, **9** (5), pp.657-677.

Oschwald, M., Schik, A. (1999) Supercritical nitrogen free jet investigated by spontaneous Raman scattering, *Experiments in Fluids*, **27**, 497-506.

Oschwald, M., Schik, A., Klar, M., Mayer., W. (1999a) Investigation of coaxial LN2-GH2-injection at supercritical pressure by spontaneous Raman scattering, *AIAA* 99-2887, 35th Joint Propulsion Conference, Los Angeles, CA.

Oschwald, M., Micci, M. (2002) Spreading angle and centerline variation of density of supercritical nitrogen jets, *Atomizations and Sprays*, **11**. pp. 91-106

Papamoschou, D. and Roshko, A. (1988) The compressible turbulent shear layer: an experimental study, *J. Fluid Mech.,* **197**, pp. 453-477

Papanicolaou, P. N. and List, E. J. (1988) Investigations of round vertical turbulent buoyant jets, *J. Fluid Mech.*, 195, pp. 341-391.

Richards, C. D. and Pitts, W. M. (1993) "Global density effects on the self-preservation behavior of turbulent free jets," J. Fluid Mech., vol. 254, pp. 417-435.

Reitz, R.D. and Bracco, F.V. (1979) On the dependence of spray angle and other spray parameters on nozzle design and operating condition, *SAE Paper* no. 790494

Schlichting, H. (1979) *Boundary Layer Theory*, MacGraw-Hill Book Company, seventh edition.

So, R M C, Zhu, J Y, Otugen, M V, and Hwang, B C, (1990) Some Measurements in a Binary Gas Jet, *Experiments in Fluids*, **9**, 273-284.

Sreenivasan, K. R. and Meneveau, C. (1986) The fractal facets of turbulence, *J. Fluid Mech.*,**173**, pp. 357-386.

Street, W.B., Calado, J.C.G. (1978) Liquid-vapor equilibrium for hydrogen and nitrogen at temperatures from 63 to 100 K and pressures to 57 MPa, *J. Chem. Therm.*, **10**, pp. 1089-1100.

Taylor, J. J. and Hoyte J.W. (1983) Water jet photography-technique and methods, *Exp. Fluids*, **1**, pp. 113-120, 1983.

Telaar, J., Schneider, G., and Mayer, W. (2000) *Experimental Investigation of breakup of turbulent liquid jets*, ILASS-Europe 2000, Darmstadt, Germany

Tseng, L.-K., Ruff, G.A., Wu, P.-K., and Faeth, G.M. (1995) Continuous- and dispersed-phase structure of pressure-atomized sprays, *Progress in Astronautics and Aeronautics: Recent Advances in Spray Combustion*

Tully, DeVaney, Rhodes (1970) Phase equilibria of the Helium-Nitrogen system from 122 to 126 K, *Advanced Cryogenic Engineering*, U.S. Bureau of Mines, **16**, 1970, pp. 88-95, Helium Research Center, Amarillo, Texas.

Wygnanski, I and Fiedler, H. E. (1970) The two-dimensional Mixing region, *J. Fluid Mech.*, **41**, 327

List of Tables

Combustor	SSME	LE-7A	Vulcain	Vinci
P/Pc	4.4	2.40	2.28	1.19

Table 1. Combustion chamber pressure of LOX/H2 engines in units of the critical pressure of oxygen

Critical Properties	N_2	He	O_2	H_2
Critical Pressure P_{crit} (MPa)	3.4	0.23	5.04	1.28
Critical Temperature T_{crit} (K)	126.2	5.2	154.6	32.94

Table 2. Critical properties of relevant fluids

	test case	v_{N2} [m/s]	T_{N2} [K]	v_{H2} [m/s]	T_{H2} [K]
single N_2-jet	A4	5	140	-	-
	B4	5	118	-	-
coaxial N_2/H_2-jet	D4	5	140	60	270
	E4	5	118	120	270
	F4	5	118	60	270

Table 3. Injection conditions for Raman scattering tests

test case	A4	B4	D4	E4	F4
$x_{1/2}$/D	9	11	3	5.5	6

Table 4. Distance where nitrogen density has decayed to 50% of its injection value.

Figures
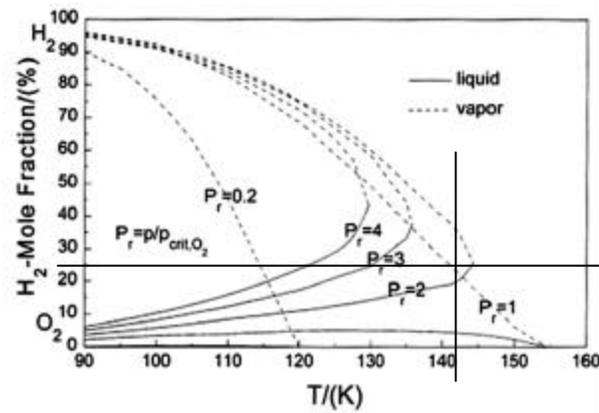
Figure 1. Phase equilibrium of the binary O_2/H_2 system. The concentration of the H_2/O_2 species is also displayed.
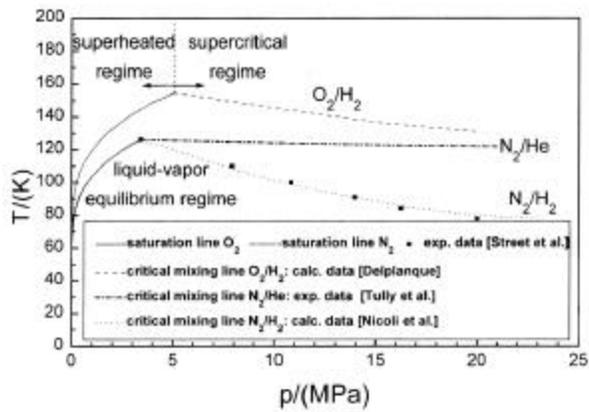
Figure 2. Critical mixing lines for binary O_2/H_2, N_2/He, and N_2/H_2-systems. Data are from Delplanque and Sirignano (1993), Nicoli et al. (1996), Street and Calado (1978), and Tully et al. (1970).
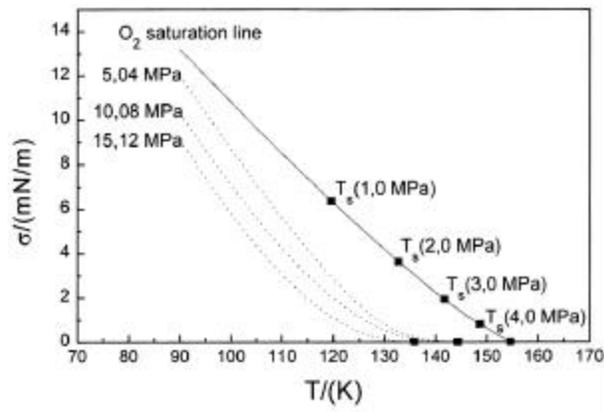
Figure 3. Phase equilibrium of the O_2/ H_2 binary system. The solid line is for pure oxygen and the dashed lines are for binary mixtures.
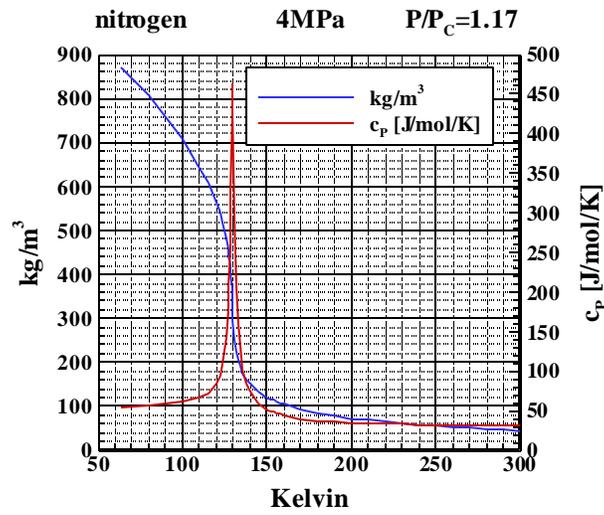
Figure 4. Density and specific heat of N_2 in the region near the critical point. The specific heat reaches a maximum at T^*=129.5K.
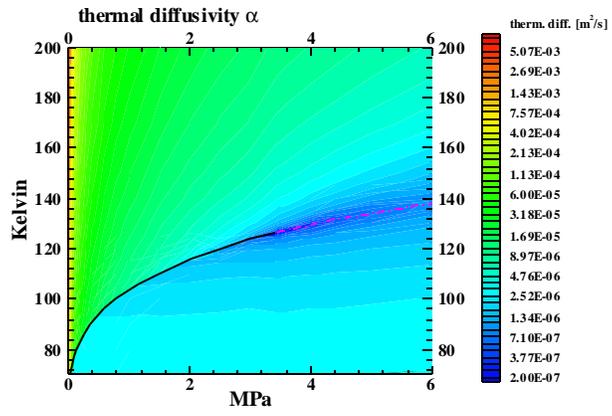
Figure 5. Thermal diffusivity of N_2 in the region near the critical point. The solid line is the two-phase coexistence line. The dashed line is the pseudo-boiling line, or T^* as a function of pressure.
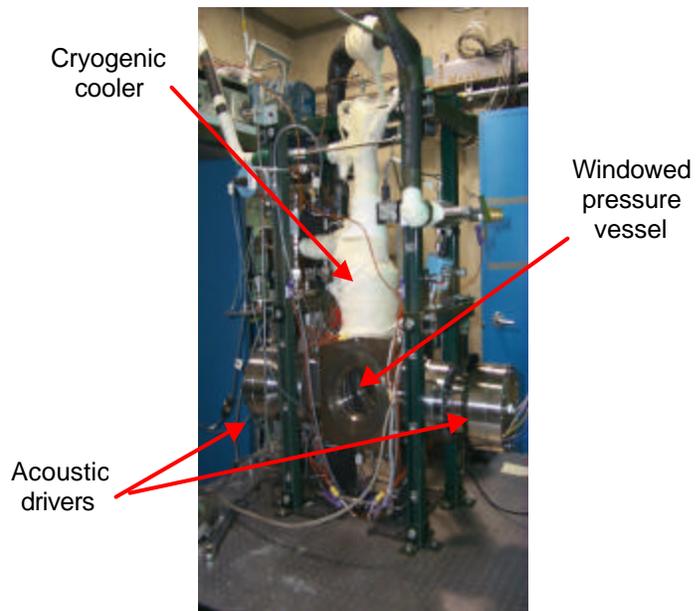
Figure 6. Test bench at AFRL.
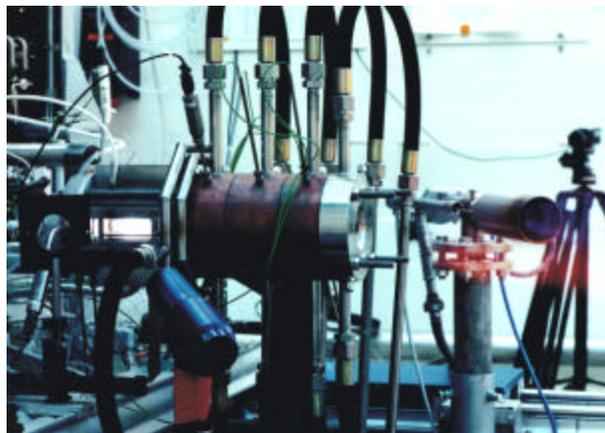
Figure 7. Windowed combustion chamber "C" with module for optical access at test bench P8.

(a)
Pr=0.91
Re=75,281

(b)
Pr=1.22
Re=66,609

(c)
Pr=2.71
Re=42,830
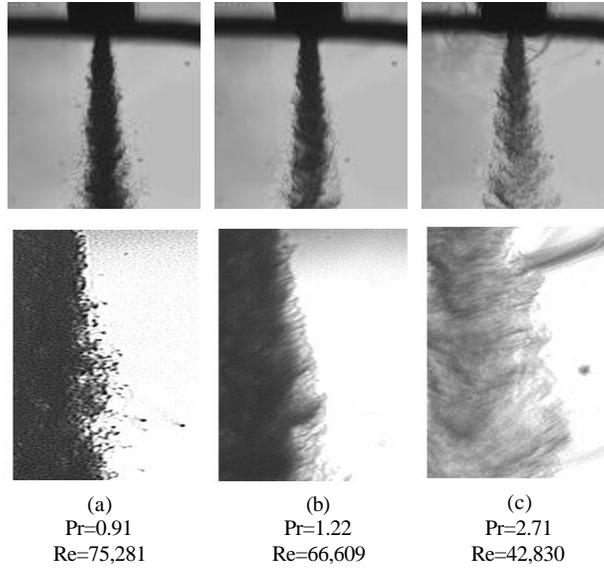
Figure 8. LN$_2$ injected into ambient temperature nitrogen at three reduced pressures ranging from subcritical to supercritical. The bottom row contains magnified images of the top row.
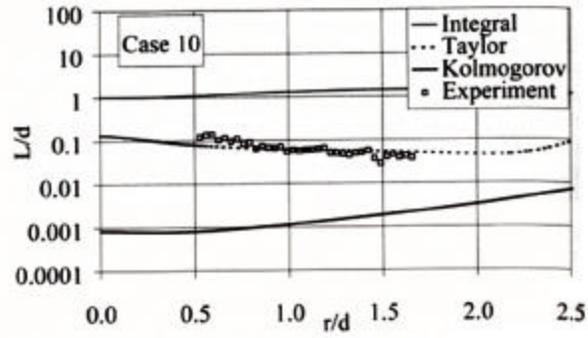
Figure 9. Comparison between calculated and experimental length scales L_{int}, L_{Kol}, L_{Tay} at x/d=10, 6MPa, 1.9m/s, T=132 K.

radial length scale (a)

axial length scale (b)
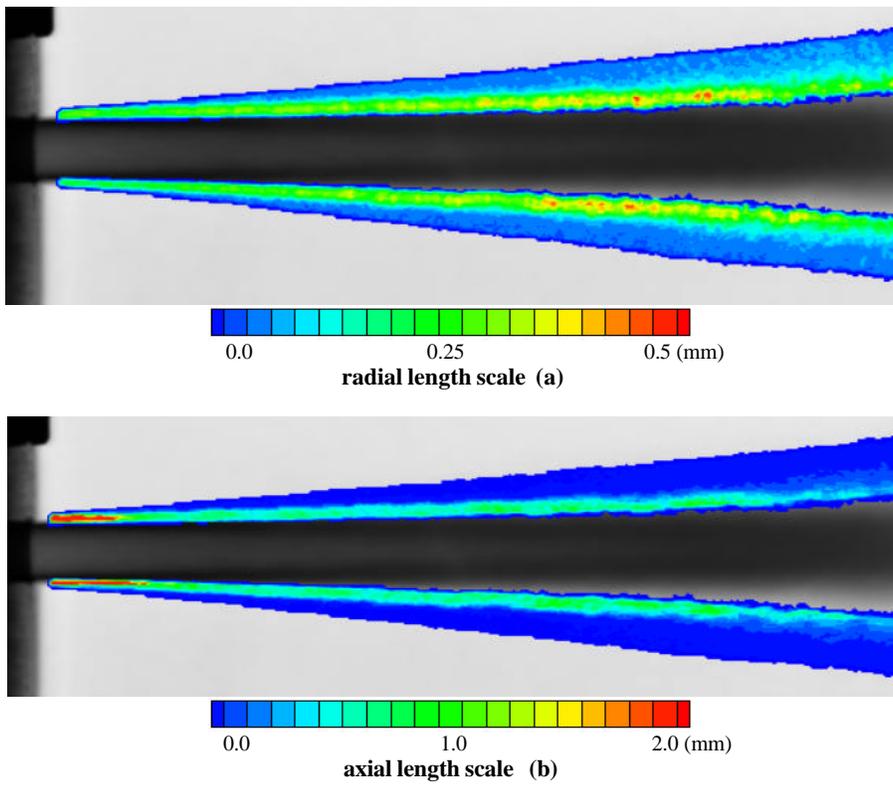
Figure 10. Experimental length scales for LN_2 into GN_2, 4MPa, 123 K.

29
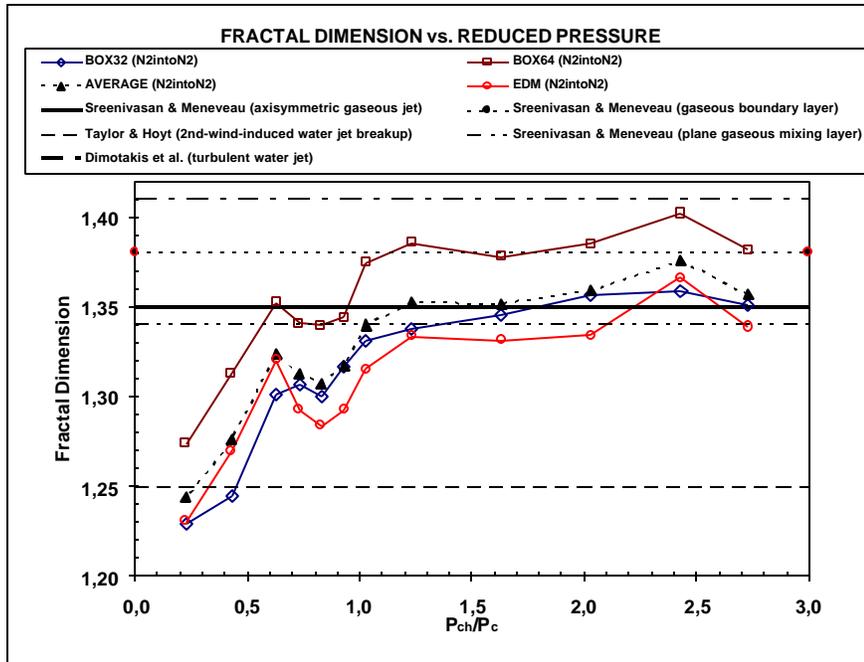
Figure 11. Fractal dimensions of the boundaries of various jets as a function of reduced pressure (chamber pressure divided by the critical pressure of the jet material). Discrete points are data from Chehroudi et al. (1999a). Box32, Box64, and EDM are different methods of calculating the fractal dimension, giving an impression of the extent of variability; for details, see Chehroudi et al. (1999a).
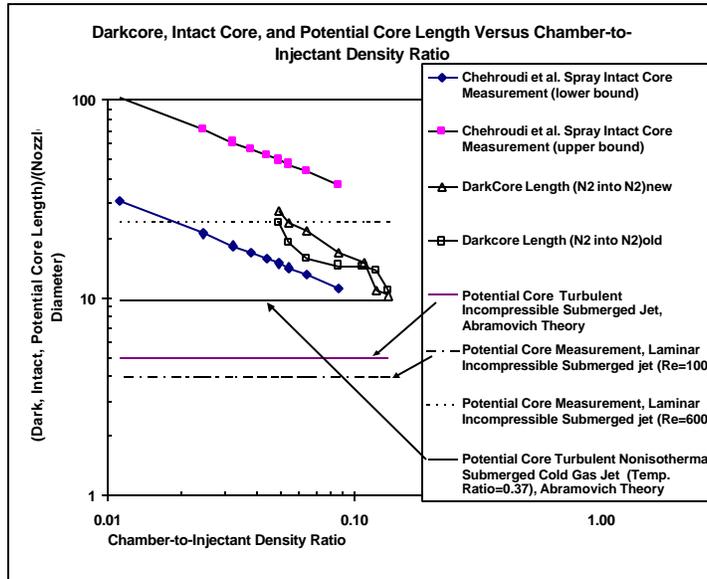
(a)
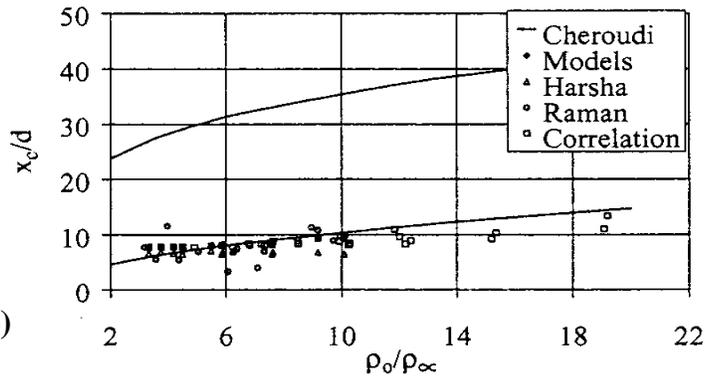
(b)

Figure 12. Ratio of either the Dark-core, intact-core, or potential-core length, depending on the case, divided by the density ratio. Case a: Chehroudi et al. (2002), determined by analysis of shadowgraphs, for an injector L/D=200. Case b: Branam and Mayer (2003), determined via Raman data, injector L/D=40. Models: determined by computer simulation. Correlation: a correlation using a set of Raman data by Branam and Mayer.

a)
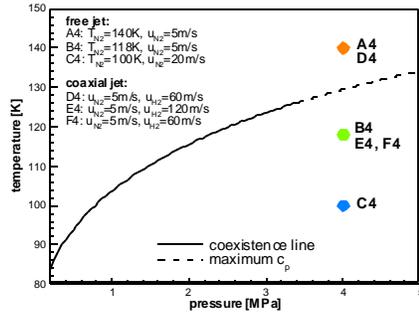
a)
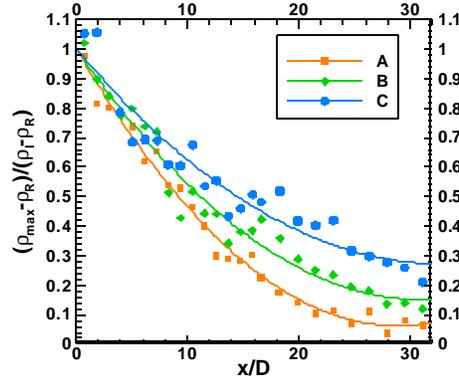
b)
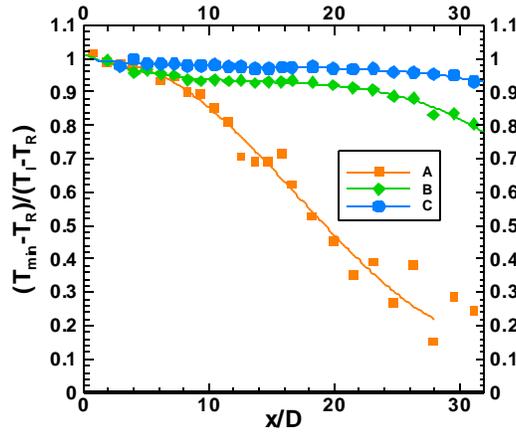
c)

Figure 13. Normalized centerline density (b) and temperature (c) axial profiles of LN$_2$ injected into GN$_2$ at three different injection temperatures and a chamber pressure of 4 MPa (i.e., near critical pressure). The plot (a) shows the thermodynamic conditions under which test cases A, B, and C are conducted. The dashed line is the pseudo-boiling line. Note, A4, B4, and C4 symbols represent A, B, and C cases, respectively.
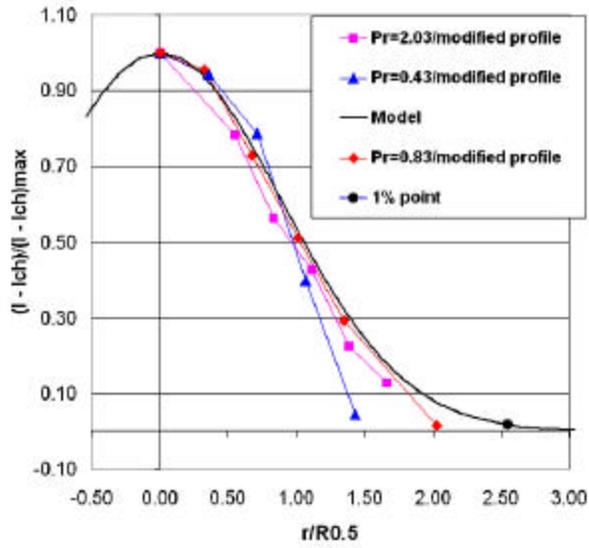
(a)
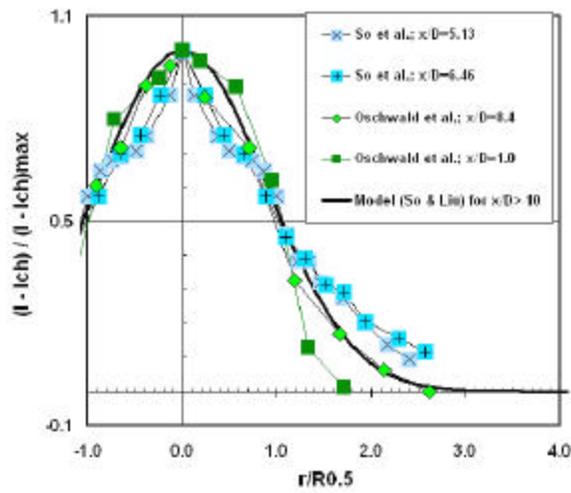
(b)

Figure 14. (a) Plots of normalized intensity vs. normalized radius for LN_2 injected into GN_2, at x/D=12.2, at subcritical, near-critical, and supercritical pressures (Chehroudi et al. (2000)). (b) Similar results by Oschwald and Schick (1999), and gaseous jet experimental data by So et al. (1990) . The solid curve is the self-similar model that represents data from a gaseous jet injected into a gaseous environment. I and Ich are measured intensities in the jet and in the chamber far away from the jet.
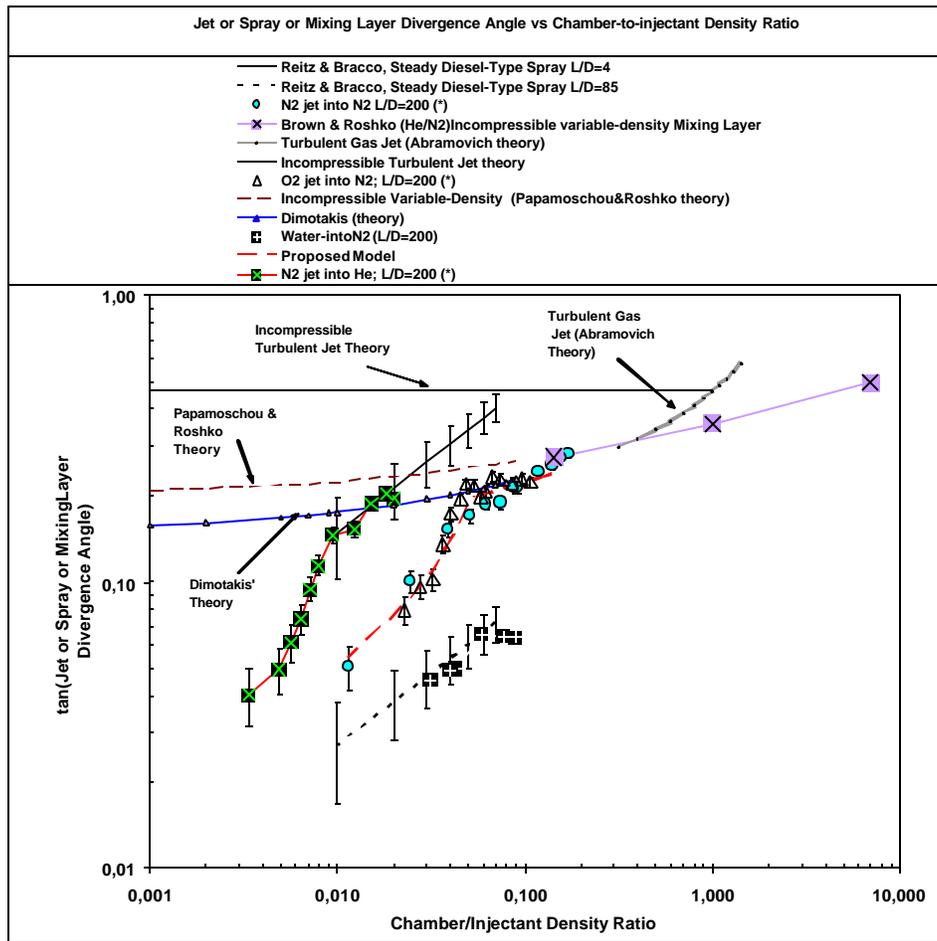
Figure 15. Spreading or growth rate as a tangent of the visual spreading angle versus the chamber-to-injectant density ratio. Data taken at AFRL are indicated by an asterisk (*) in the legend.
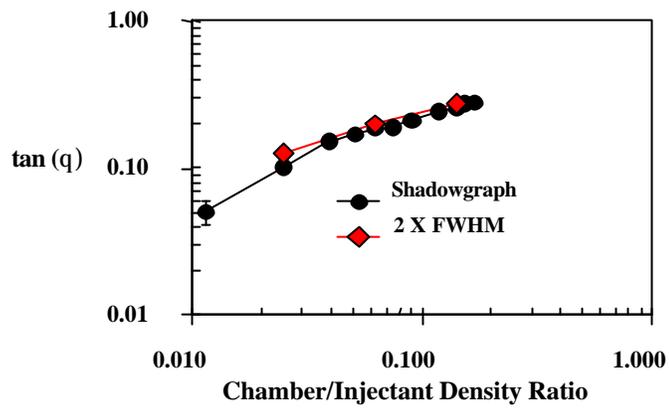
Figure 16. Comparison of the tangent of the spreading angle measured using shadowgraph and Raman techniques using twice the FWHM values.
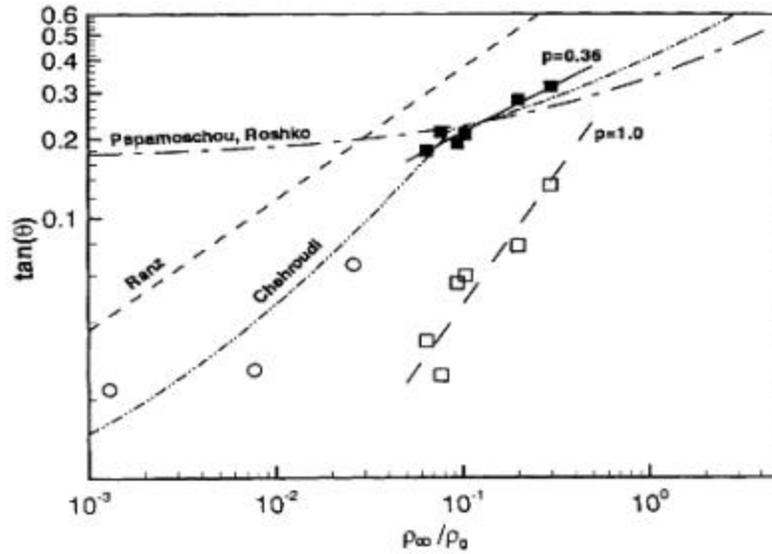
Figure 17. Comparison of the tangent of the spreading angle by Raman techniques using twice the FWHM values (DLR data). Solid squares are for data from x/D of 15 to 32 whereas hollow squares are from x/D of 0.5 to 14. Chehroudi's model is also shown as dash-dot-dot curve. LN_2 into GN_2 with injector L/D=11.6. Data from Oschwald and Micci (2002). Open circels are data points from R.D. Reitz and F.V. Bracco (1979).
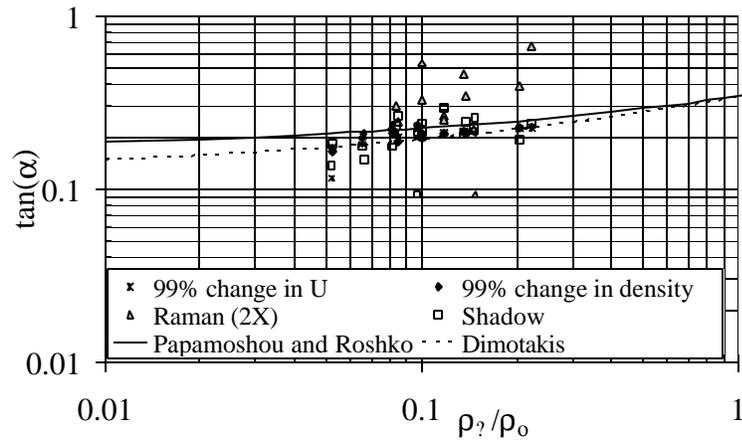
Figure 18. Comparison of the tangent of the spreading angle measured using shadowgraph and Raman techniques using twice the FWHM values and computer simulation (DLR data). LN_2 into GN_2 with injector L/D= 40. Data by DLR, Branam and Mayer (2003).
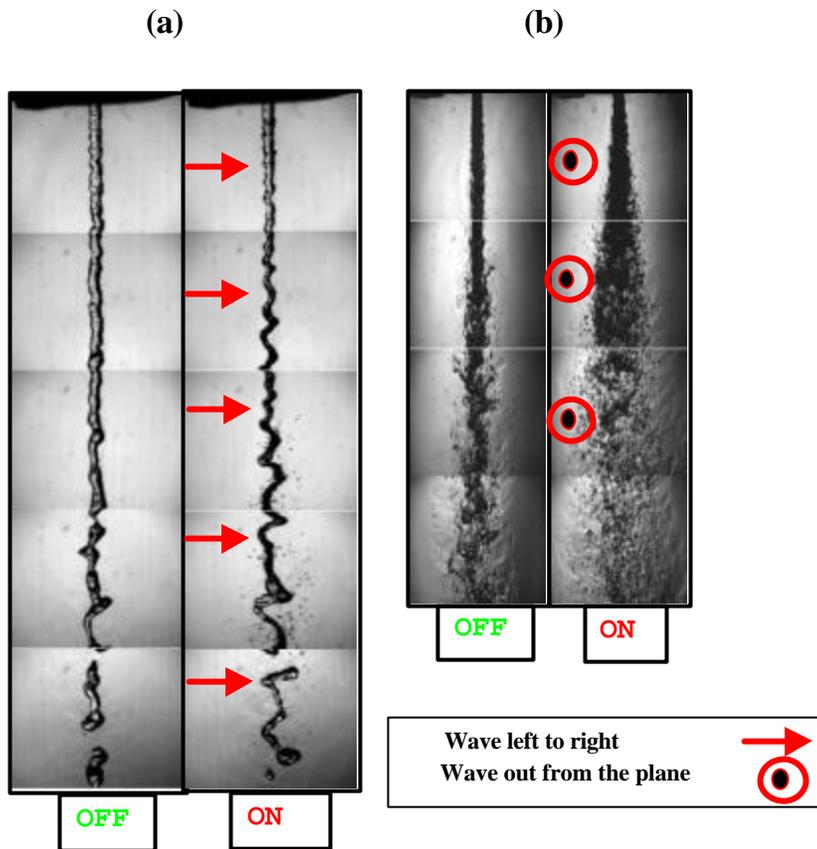
Figure 19. Interaction of acoustic waves with a single LN_2 jet injected into GN_2 at subcritical pressure. "ON" and "OFF" indicate the state of the acoustic driver. (a) front view and (b) side view.
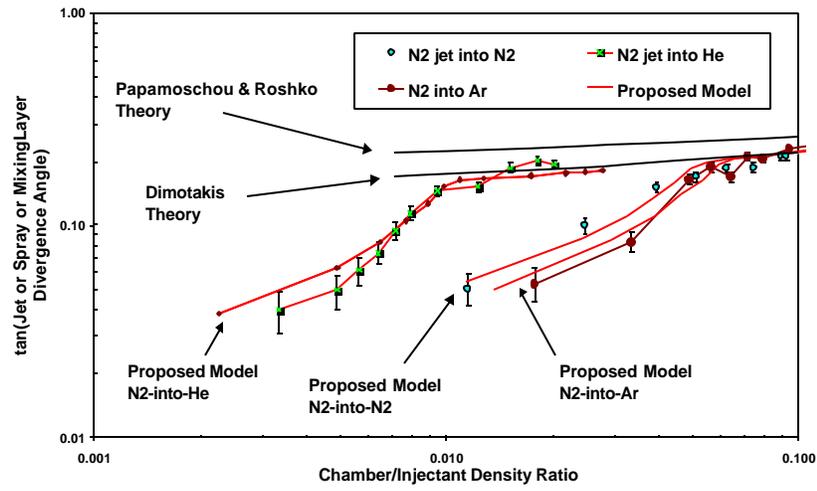
Figure 20. Comparison of the proposed growth rate model with experimental data.
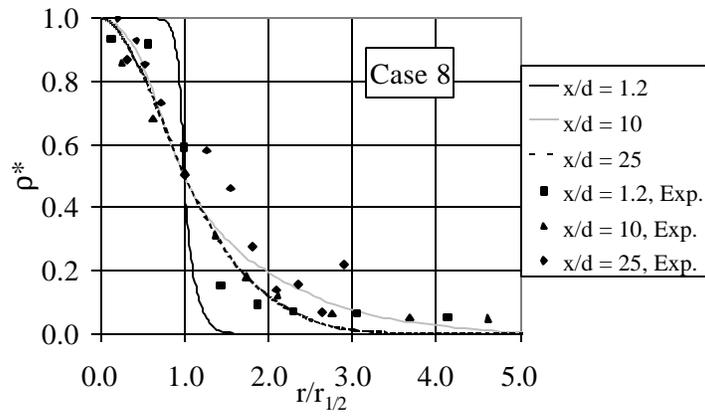
Figure 21. Density; 5.0 MPa, 123 K, 2.0 m/s.
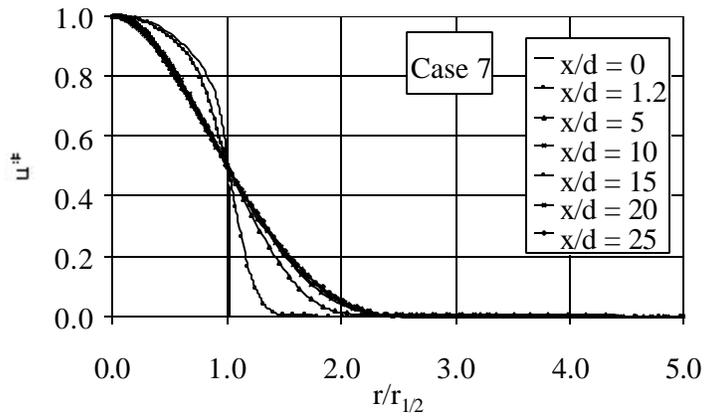
Figure 22. Velocity; 4.9 MPa, 104 K, 1.8 m/s.
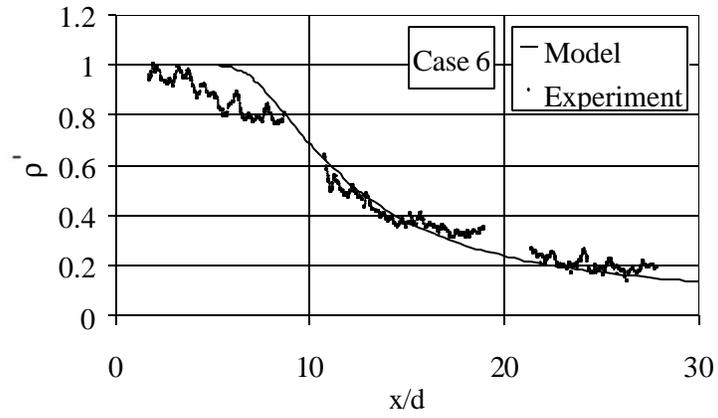
Figure 23. Centerline density; 3.9 MPa, 133 K (above the pseudo-boiling line), 5.4 m/s.
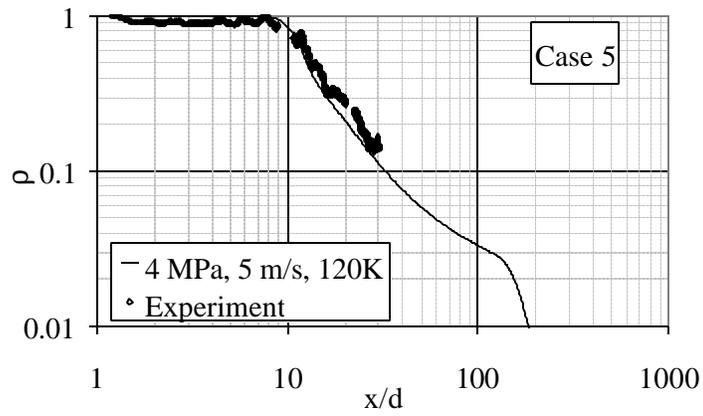
Figure   24. Centerline density; 4.0 MPa, 123 K (below the pseudo-boiling line), 4.9 m/s.
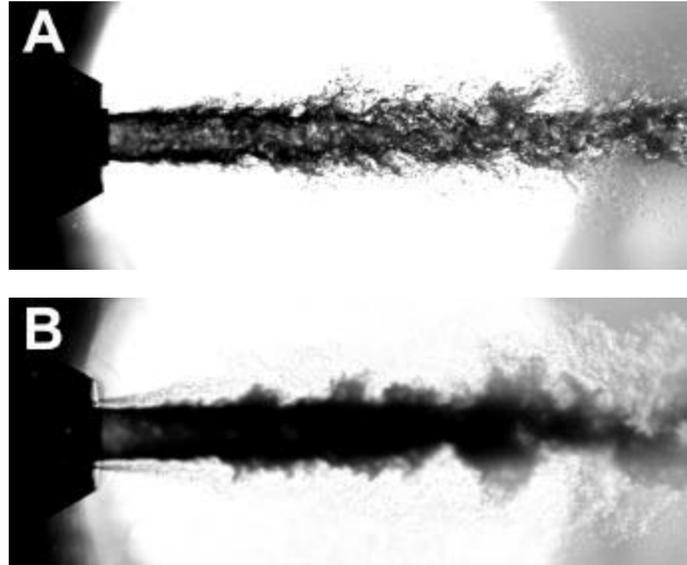
Figure 25. Binary liquid N_2/GHe system at A: 1.0 MPa, B: 6.0 MPa. d_{LN2} = 1.9 mm, v_{LN2} = 5 m/s, v_{He} = 100 m/s, T_{LN2} = 97 K, T_{He} = 280 K (from Mayer and Smith, in press).

(a)

(b)
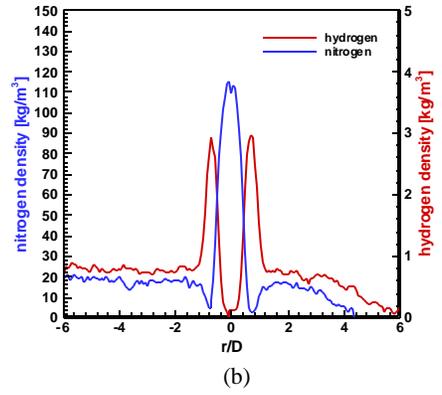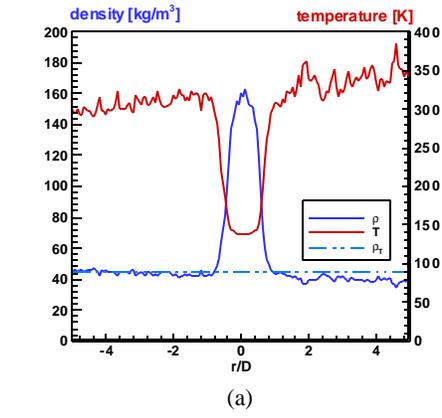
Figure 26. (a) Radial N_2 density profile for test case A4 (single jet), 2mm (x/D=1.05) downstream of the injector exit. (b) Radial N_2 and H_2 density profiles for coaxial LN_2/ H_2 injection for test case D4, 2mm (x/D=1.05) downstream the injector exit. Laser beam direction is from left to right.
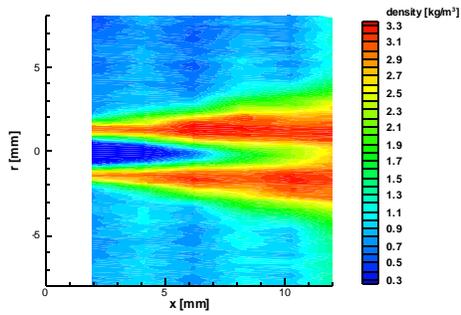
Figure 27. H_2 density for coaxial LN_2/H_2 injection for test case D4 (T_{N2} = 140K, T_{H2} = 270K).
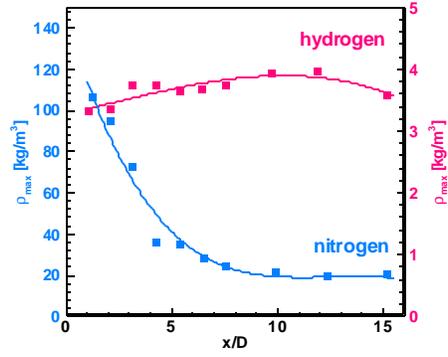
Figure 28. Evolution of the maximum nitrogen and hydrogen density downstream of the injector for test case D4.
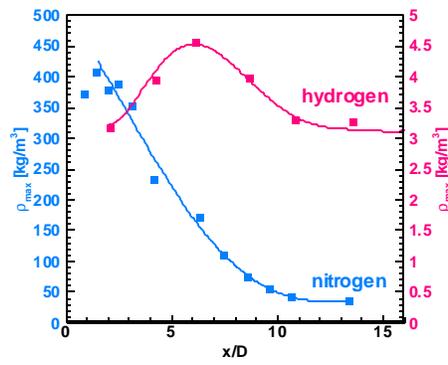
**Figure 29.** Evolution of the maximum nitrogen and hydrogen density downstream of the injector for test case E4.
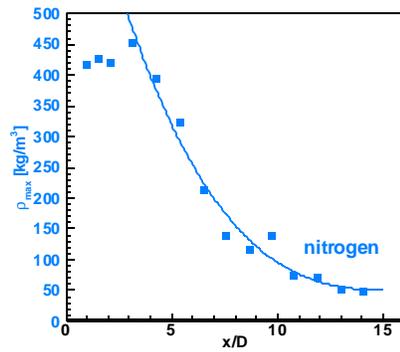
44

(a) Subcritical Pressure, 1.5 MPa Combustion
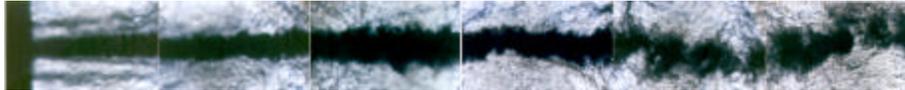
(b) Supercritical Pressure, 10 MPa Combustion

Figure 31. Combustion of the LOX jet at subcritical (a) and supercritical (b) pressures, from Mayer and Tamura (1996).
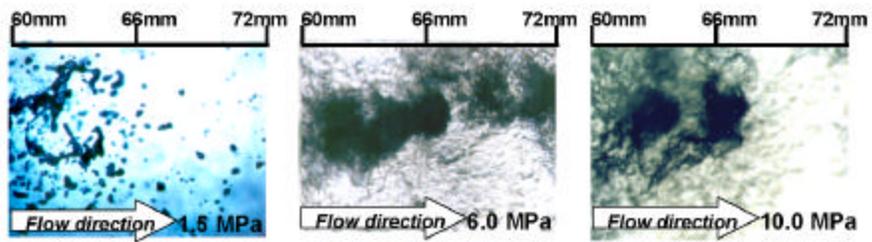

Figure 32. Visualization of O_2-jet disintegration with varying chamber pressure (Mayer and Smith (in press)).